Journal of Nanobiotechnology

RESEARCH Open Access

Decellularized tissue matrices hydrogels functionalized with extracellular vesicles promote macrophage reprogramming and neural stem cell differentiation for spinal cord injury repair

Ming Deng[1], Ping Xie[2], Hongyang Xue[3], Qing Chen[1], Yan Zhou[1], Jianghua Ming[1], Yonggang Ma[1], Junqi Liu[4] and Hui Huang[5*]

Abstract

This study investigates the application of decellularized tissue matrices (DSCM) hydrogels functionalized with extracellular vesicles (EVs) derived from mesenchymal stromal cells (MSCs) for spinal cord injury (SCI) treatment. The primary focus is on how these composites influence macrophage reprogramming and neural stem cell (NSC) differentiation by modulating Slamf9 expression. MSC-derived EVs were successfully isolated, and DSCM hydrogels were prepared from porcine spinal cords. The composite material, EVs derived from MSCs (DSCM@EVs), was constructed and applied to a mouse SCI model, showing significant enhancement in NSC differentiation and axonal growth, thereby alleviating SCI. Bioinformatics and in vitro cell experiments revealed that DSCM@EVs promote the reprogramming of M1 macrophages to the M2 phenotype, reducing inflammatory responses and facilitating NSC differentiation. RNA-seq analysis identified Slamf9 as a key regulatory gene, with its suppression linked to the observed therapeutic effects. This novel approach demonstrates the potential of DSCM@EVs in SCI repair by modulating the inflammatory environment and promoting neural regeneration, offering a promising strategy for treating SCI and potentially other inflammatory neurological disorders.

Keywords Spinal cord Injury, Decellularized tissue matrices Hydrogels, Extracellular vesicles, Macrophage reprogramming, Neural stem cell differentiation

Ming Deng and Ping Xie are Co-first authors.

*Correspondence:
Hui Huang
120653927@hainmc.edu.cn
[1]Department of Orthopedics, Renmin Hospital of Wuhan University, Wuhan 430060, China
[2]Department of Chinese Traditional Medicine, Tongren Hospital of Wuhan University (Wuhan Third Hospital), Wuhan 430060, China
[3]The First Clinical College of Wuhan University, Wuhan 430060, China
[4]Department of Radiation Oncology, The First of Affiliated Hospital of Zhengzhou University, Zhengzhou 450000, China
[5]Department of Sports Medicine, Hainan General Hospital (Hainan Affiliated Hospital of Hainan Medical University), Haikou, Hainan Province 570311, China

Introduction

Spinal cord injury (SCI) is a debilitating condition that significantly impacts individuals' quality of life, potentially leading to loss of limb function as well as affecting physiological functions such as respiration and excretion [1]. Despite notable advancements in scientific research and medical technologies, effective treatments for SCI remain limited [2]. Surgical procedures and pharmaceutical interventions typically only slow symptom progression and often fall short of achieving complete functional recovery [3]. This is primarily due to the permanent loss of neurons following SCI and the disruption of the microenvironment, particularly the neural stem cells (NSCs) microenvironment [4, 5]. Therefore, the effective promotion of neuronal and microenvironment repair is a crucial direction in current SCI treatment research.

Mesenchymal stromal cells (MSCs) are considered a promising means of neurorepair due to their multipotent differentiation potential and immunomodulatory characteristics [6, 7]. In recent years, researchers have discovered that extracellular vesicles (EVs) secreted by MSCs also possess the ability to promote tissue repair and immunoregulation [8]. EVs not only carry various bioactive molecules but also exhibit excellent biocompatibility and stability, leading to their increasing application in therapeutic models of various diseases [9–11]. Particularly in neurological disorders, EVs derived from MSCs (DSCM@EVs) have demonstrated favorable therapeutic effects in animal models and clinical studies [12].

DSCM are biocompatible materials that provide a natural growth environment for cells by removing cellular components while retaining the extracellular matrix structure [13]. DSCM has achieved successful application in tissue engineering fields such as skin, bones, and heart [14]. In the realm of neural repair, DSCM can serve as an ideal carrier to deliver MSCs or their EVs into the injury site, thereby enhancing the repair of neural and microenvironmental elements more effectively [13, 15, 16].

Based on this background, the aim of our study is to explore the potential application of MSC-derived EV-functionalized DSCM hydrogels (DSCM@EVs, Decellularized tissue matrices (DSCM) hydrogels loaded with EVs derived from MSCs) in treating SCI, particularly focusing on how they influence the reconstruction of the NSC microenvironment through regulation of Slamf9 expression in macrophages. By combining bioinformatic analyses with in vitro and in vivo experiments, we uncovered the molecular mechanisms through which DSCM@EVs promote SCI repair. This novel therapeutic strategy not only offers a promising approach for SCI treatment but may also have positive implications for the treatment of other neurological diseases. The findings of this study hold significant scientific and clinical value in addressing the substantial medical challenges posed by SCI.

Materials and methods

Ethical declaration

This research has obtained approval from the Ethics Committee of Renmin Hospital of Wuhan University and strictly adheres to the ethical standards and guidelines of the Helsinki Declaration. Prior to conducting in vivo animal experiments, we ensure the scientific value of the research and strive to minimize harm and suffering to the animals. We make every effort to use the fewest animals possible and take all necessary measures during the experiments to reduce pain and distress, such as using anesthetics and analgesics or providing appropriate housing conditions. We commit to strictly adhere to relevant laws, regulations, and ethical guidelines, such as the Animal Welfare Act and other related provisions.

Public Data download and batch Processing

Data sets GSE5296 and GSE47681 related to SCI were downloaded from the Gene Expression Omnibus (GEO) database (http://www.ncbi.nlm.nih.gov/geo/). Specifically, 14 Sham group samples (GSM119812, GSM119844, GSM119833, GSM119834, GSM119781, GSM119845, GSM119820, GSM119813, GSM119796, GSM119782, GSM119801, GSM119797, GSM119767, GSM119802) and 18 SCI group samples (GSM118664, GSM118672, GSM119764, GSM119811, GSM120018, GSM119779, GSM119830, GSM119794, GSM119765, GSM119780, GSM119800, GSM119766, GSM119818, GSM119819, GSM119795, GSM119831, GSM119843, GSM119832) from the GSE5296 dataset were selected. Moreover, 4 Sham group samples (GSM1154538, GSM1154539, GSM1154540, GSM1154542) and 13 SCI group samples (GSM1154520, GSM1154521, GSM1154522, GSM1154523, GSM1154529, GSM1154530, GSM1154531, GSM1154532, GSM1154533, GSM1154541, GSM1154547, GSM1154548, GSM1154549) from the GSE47681 dataset were included. Subsequently, the "limma" and "sva" packages were utilized to merge the GSE5296 and GSE47681 datasets and perform batch correction. After correction, the combined data was visualized using the "ggplot2" package for principal component analysis (PCA) assessment [17–19].

Analysis of immune cell infiltration in public data

The expression matrix of 22 immune cell characteristic gene sets was downloaded from the CIBERSORT website. The CIBERSORT algorithm was utilized to analyze immune cells in the merged GSE5296 and GSE47681 datasets, with 1000 simulation iterations, filtering out non-infiltrating immune cells. Relations between target genes and different immune cells were examined using the R script "CIBERSORT," and the correlation between core gene expression and SCI immune cell infiltration was analyzed [20]. A co-expression network was

constructed using the "WGCNA" package in R software. The workflow involved building the gene co-expression network, module identification, module relationship analysis, and identification of highly correlated genes. A soft threshold parameter $\beta = 3$ and scale-free $R^2 = 0.90$ were set, and the module most significantly associated with M1 macrophage infiltration was selected as the key module for M1 macrophage infiltration, with the genes from this module obtained for subsequent analysis [21, 22].

Identification of differentially expressed genes in public data

In this study, we performed a differential expression analysis of genes in the merged dataset using the "limma" package in R. We identified differentially expressed genes with a significant p-value of less than 0.05. Furthermore, we generated a volcano plot of the differentially expressed genes using R language [23].

Identification of BMSCs

Healthy mouse BMSCs (catalog number: CP-M131, Procell, China) were cultured in α-MEM medium (SH30265.01, HyClone, Thermo Fisher Scientific, USA) supplemented with 15% fetal bovine serum (FBS; 10091148, Thermo Fisher Scientific, USA) and 100 U/mL penicillin-streptomycin solution (10378016, Thermo Fisher Scientific, USA). Upon reaching 80% confluence, the third passage (P3) BMSCs was used for subsequent experiments.

Cells were washed with PBS and resuspended in a single-cell suspension at a concentration of 1×10^6/mL. Fluorescently labeled antibodies, including CD44 (ab243894), CD73 (ab288154), CD90 (ab3105), CD105 (ab221675), CD45 (ab10558), and CD31 (ab7388), were added based on grouping requirements. Following a 30-minute incubation at 4 °C, unbound antibodies were washed off with PBS, and the expression of corresponding labeled antibodies in the samples was analyzed using a flow cytometer. Antibodies used for phenotypic-related assays were all purchased from Abcam (UK).

Following the instructions of the BMSCs induction differentiation (osteogenic, adipogenic, and chondrogenic) assay kit (PD-003/4/5, Procell, China), Safranin O, Oil Red O staining, and Alcian Blue staining were respectively used to observe BMSCs' osteogenic, adipogenic, and chondrogenic differentiation capabilities [24].

Isolation, purification, and identification of EVs

Third passage (P3) BMSCs were cultured until they reached 80–90% confluence. The culture medium was removed, and the cells were washed twice with PBS. Subsequently, they were incubated in a 10% FBS medium to deplete EVs in a 37 °C, CO_2-regulated incubator for 48 h. After collecting the supernatant, centrifugation was performed at 500 g for 15 min at 4 °C to eliminate cellular debris. This was followed by centrifugation at 2000 g for 15 min at 4 °C to remove cell fragments or apoptotic bodies and then at 10,000 g for 20 min at 4 °C to eliminate large vesicles. The centrifuged samples were filtered through a 0.22 μm filter and further centrifuged at 110,000 g for 70 min at 4 °C. Subsequently, the samples were resuspended in PBS and subjected to another high-speed centrifugation under the same conditions. Finally, the pellets were resuspended in 100 μL of sterile PBS for downstream experiments. All high-speed centrifugation procedures were performed at 4 °C using a Beckman ultracentrifuge (Optima L-90 K, Bio-thing, China) equipped with an SW-32Ti rotor. The remaining low-speed centrifugation steps were carried out using a Beckman Allegra X-15R (Beckman Coulter) benchtop centrifuge.

EVs were analyzed using a NanoSight Nanoparticle Tracking Analyzer (Malvern Instruments Ltd, Malvern Panalytical, France). Twenty micrograms of EVs were dissolved in 1 mL of PBS and vortexed for 1 min to ensure even distribution, and then the particle size distribution of EVs was directly observed and measured.

For transmission electron microscopy (TEM) analysis, 20 μL of EV samples were loaded onto carbon-coated copper electron microscope grids, allowed to stand for 2 min, and then negatively stained with phosphotungstic acid solution (12501-23-4, Sigma-Aldrich, USA) for 5 min. Subsequently, the grids were washed three times with PBS to remove excess phosphotungstic acid solution and partially dried with filter paper. EV images were observed at 80 kV using a Hitachi H7650 transmission electron microscope (DOLEE, Japan).

The EV suspension was concentrated, and its protein content was determined using the BCA assay kit (23227, Thermo Fisher Scientific, USA) according to the manufacturer's instructions. The surface markers of EVs were then identified by Western blot, specifically detecting the expression of EV-specific marker proteins HSP70, CD9, CD81, and Calnexin [24, 25].

Preparation of DSCM

A 48 kg miniature pig was purchased (Hubei Offspring Biotechnology Co., Ltd., China), and the fresh spinal cord with attached dura mater was carefully harvested. The spinal cord was decellularized using a solution of 3% v/v Triton X-100 and 4% v/v sodium deoxycholate for 12 h, followed by rinsing with sterile water at 4 °C. After decellularization, the spinal cord was defatted with 4% v/v ethanol. The decellularized spinal cord and surrounding nerve tissues were then treated in a solvent mixture (dichloromethane = 2:1, v/v), freeze-dried, and ground into a powder. The DSCM powder was subsequently

digested in an acidic solution of 0.01 M hydrochloric acid containing pepsin (1 mg/mL) at 25 °C for 12 h. Centrifugation was performed at 50,000 g for 30 min at 4 °C to remove residual particles. The pH of the digest was adjusted to 7.4 using 1 M NaOH, and the solution was equilibrated with 10× PBS before allowing it to sit at 37 °C for a few minutes to form the DSCM gel [13, 26]. The final DSCM hydrogel (1 mg/mL concentration) was stored at -20 °C.

Characterization of DSCM

To confirm the extent of decellularization, we assessed residual DNA in native spinal cord tissue and decellularized spinal cord tissue using the DNeasy kit and H&E staining. Samples were enzymatically digested with Proteinase K, followed by DNA extraction using the Sigma DNA extraction kit (G1N70, USA). Subsequently, DNA content was quantified using the Quant-iT™ PicoGreen™ dsDNA assay kit (P11496, Thermo Fisher Scientific, USA) on a Synergy H4 microplate reader (Biotek, USA) at excitation and emission wavelengths of 480 nm and 520 nm, respectively, with triplicate measurements for each group. For H&E staining, native and decellularized spinal cord tissues were fixed in 4% paraformaldehyde, washed thrice with distilled water, embedded in optimal cutting temperature compound (OCT, SAKURA, Netherlands), and sectioned using a Leica CM1850 Cryostat (Germany). The tissue sections were stained with Hematoxylin and Eosin (H&E) using the Beyotime staining kit (C0105, China) and observed with an AxioScan microscope (Zeiss, Germany).

The ultrastructure of the hydrogel was observed using scanning electron microscopy (SEM). Samples were prefixed in 2.5% glutaraldehyde for 6 h, washed thrice with deionized water for 30 min each, dehydrated in a series of ethanol solutions (30%, 50%, 75%, and 100%) for 30 min per step, then soaked in deionized water for 6 h (changing water every 2 h), followed by freeze-drying. The freeze-dried samples were quenched rapidly in liquid nitrogen and fractured before the characterization of the hydrogel samples using a scanning electron microscope (HITACHI S-4800, Japan) at 10 kV. The nano-fiber diameter and porosity of each sample were measured using ImageJ 1.52a.

The hydroxyproline assay was used to quantify residual collagen content in DSCM and DNM (Decellularized Native Matrix). Hydroxyproline concentration was determined using a standard curve of trans-4-hydroxy-L-proline (H54409, Sigma-Aldrich, USA), and the total collagen content was calculated based on a hydroxyproline-to-collagen ratio of 1:7.69. The sGAG content in DSCM was measured using a tissue sGAG quantification kit (GENMED, GMS, China, GMS19239.2) based on 1,9-dimethylmethylene blue staining. Additionally, Western blot analysis was conducted to detect tissue-specific ECM protein components, including collagen, the tenascin family (TNC), growth factor fibroblast growth factor (FGF2), and laminin [13].

Preparation, characterization, and EVs Release Profile of DSCM@EVs

DiR (D12731, Thermo Fisher Scientific, USA) was added to the EV solution at a concentration of 1:400 and incubated for 30 min, followed by ultracentrifugation at 100,000 g for 90 min to remove excess dye. The EVs were then dissolved in the DSCM solution at room temperature, allowing passive adsorption of EVs onto DSCM to form DSCM@EVs (containing EVs at 1 μg/μL). Fluorescence confocal microscopy confirmed the loading of EVs onto DSCM.

EVs release curve of DSCM@EVs: The DSCM@EVs labeled with 1 μg/μL DiR-tagged EVs were dissolved in 1 mL PBS solution at 37 °C, with daily solution replacement over 14 days. The fluorescence assay was employed to measure the release of EVs at each time point. Furthermore, on the first day, EVs were extracted for TEM morphology observation, and Western blot analysis was carried out to examine the expression of EV markers [26, 27].

Culture and characterization of NSCs and macrophages

NSCs were isolated from the spinal cords of neonatal C57BL/6 N mice (strain code: 213, Beijing Vital River Laboratory Animal Technology Co., Ltd., China). After carefully removing the meninges, spinal cord tissues were cut into 1 mm^3 pieces and digested with TrypLE Express enzyme (12604013, Gibco, USA), diluted with an equal volume of PBS (1:1), at 37 °C for 15 min. The enzyme was then further diluted with PBS, and the cells were collected by centrifuging at 500 g for 5 min. Cells were resuspended in serum-free DMEM/F12 medium containing 20 ng/mL bFGF, 20 ng/mL EGF, and 2% B27, with half of the medium replaced every three days. After 10 days, the newly formed neurospheres were digested into single NSCs as follows: sterile 10 mL centrifuge tubes were prepared, and cells were transferred to the tubes; neurospheres were allowed to settle to the bottom of the tubes by standing vertically for 15–30 min. The supernatant was removed, and 3 times the volume of Acutase digestion solution was added to the pellet, and incubated in a 37 °C water bath for 5 min. The neurospheres were gently dissociated into a single-cell suspension using a finely polished glass pipette (this step did not exceed 5 min). Cells were counted and cultured in an adhesive medium containing 10% fetal bovine serum at a concentration of 5×10^5 cells/mL. NSCs were cultured in poly-D-lysine-coated 24-well plates at a density of 1×10^5 cells/well and then differentiated using neuronal induction

medium (NIM), which consisted of DMEM/F12 medium, 2% B27, and small molecules (3 μM CHIR99021, 5 μM SB431542, 0.25 μM LDN193189, 3 μM P7C3, 1 μM DAPT, 5 μM ISX9, 0.5 μM purmorphamine, 1 μM dorsomorphin, 1 μM SU5402, 0.5 μM Repsox, 10 μM RG108, 0.5 mM VPA, 10 μM forskolin). Half of the medium was replaced with fresh medium every two days. NSCs were observed under a standard optical microscope, and the purity of NSCs was assessed via immunofluorescent co-staining for Nestin and SOX2 expression [28–30].

Co-culture of DSCM@EVs and M1 macrophages

This study aims to investigate the influence of DSCM@EVs on M1 macrophage reprogramming. DSCM@EVs solution was added to a 48-well culture plate, covering the bottom of each well with approximately 10 μL/cm² to create a hydrogel substrate. Bone marrow-derived macrophages (BMDMs) were then cultured on the hydrogel at a density of 3×10^3 cells per well for 3 days. The BMDMs were polarized towards the M1 phenotype by adding 20 ng/mL IFN-γ (Peprotech) and 100 ng/mL LPS (Sigma-Aldrich) to the culture medium, and then were incubated for 5, 24, and 48 h. The expression of M1 macrophage markers (Cd86, Ccr7, and Nos2) and M2 macrophage markers (Cd206, Arg1, and Il-10) was assessed by RT-qPCR at these time points, as reported in previous studies [29, 30].

Transfection of M1 macrophages

To transfect M1 macrophages, lentiviral particles carrying Slamf9 overexpression (oe-Slamf9) or negative control (oe-NC), as well as lentiviral particles carrying Slamf9 knockdown (sh-Slamf9) or negative control (sh-NC), were packaged into HEK-293T cells (CL-0005, Procell, China) at a final concentration of 100 nM of shRNA. The lentiviral interference vector used was pGreen-Puro (CMV) shRNA Lentivector (sh-, catalog number: SI505A-1, System Biosciences, USA), and the lentiviral overexpression vector was pCDH-CMV-MCS-EF1α-copGFP (Lv-, catalog number: CD511B-1, System Biosciences, USA). The silencing sequences are detailed in Table S1. Forty-eight hours post-transfection, viral supernatants were collected and concentrated by Genechem (Shanghai, China). M1 macrophages were cultured to approximately 50% confluence and then infected with lentivirus (1×10^8 TU/mL). After 48 h of infection, cells were subjected to selection with 10 μg/mL puromycin (Sigma-Aldrich, USA) for at least a week to establish stable transfected cell lines [31–33].

Co-culture of NSCs with conditioned media (CM) from M0-M2 macrophages

After 24 h of stimulation, M0, M1, and M2 macrophages were collected, supernatants were removed, and cells were washed twice with PBS. Subsequently, an equal volume of fresh neural basal medium was added to the macrophage culture media of each group, followed by incubation for another 24 h. The collected supernatants served as a neural basal medium, supplemented with penicillin/streptomycin (100 μg/ml, 15140148, Gibco, USA), L-glutamine (10 mmol/l, 21051024, Gibco, USA), B-27 supplement (20 μl/ml, A3582801, Gibco, USA), EGF (5 ng/ml, SRP3196, Sigma-Aldrich), and FGF (5 ng/ml, SRP4057, Sigma-Aldrich), yielding the conditioned media for each group of macrophages: M0-CM, M1-CM, and M2-CM. NSCs were then cultured in M0-CM, M1-CM, and M2-CM to assess proliferation, migration, differentiation, and axon formation [30].

Toxicity effects of DSCM@EVs detected by live-dead cell staining on NSCs and macrophages

NSCs and macrophages cultured in DSCM@EVs for 24 h were washed with PBS and further incubated at 37 °C in a 5% CO_2 environment with Calcein-AM/ethidium (Calcein-AM/PI Invitrogen) for 20 min as previously described [34]. Following two subsequent washes, live-dead cell status was observed using an inverted fluorescence microscope (Olympus IX71, Olympus Co., Tokyo, Japan).

Detection of NSCs proliferation by EdU Staining and CCK-8 assay

The Cell Counting Kit-8 (40203ES60, Yeasen, Shanghai, China) was employed. In brief, NSCs were cultured in conditioned media with different treatments for proliferation assessment on days 1, 3, and 7. After culturing NSCs for 3 h in media containing CCK-8 (1:10), 100 μL of the supernatant was transferred to a 96-well culture plate. The absorbance of the solution was measured at a wavelength of 450 nm using a microplate reader (EON, Gene Limited) [13, 34].

Under the same treatment conditions, on day 7, the proliferation of NSCs was assessed using the EdU assay kit (C10310-3, RiboBio, China).

NSCs migration experiment

To assess the impact of DSCM@EVs on the in vitro migration of NSCs, NSCs were cultured in conditioned media from macrophages subjected to different treatments and then incubated at 37 °C for 24 h. Subsequently, images of each well were captured using a Leica DMi8 wide-field microscope. The migration index was defined as the total area covered by migrating cells divided by the internal area of NSCs neurospheres. The internal and total areas of neurospheres were measured using ImageJ software [35].

Establishment of SCI mouse model

Forty-eight C57BL/6 N mice (8 weeks old, 20–25 g) were purchased from Beijing Vital-Hua Experimental Animal Co., Ltd. (strain code: 213, Beijing, China). The mice were housed in separate cages in an SPF-grade animal facility with a humidity of 60–65% and a temperature maintained at 22–25 °C. They were provided with ad libitum access to food and water under a 12-hour light-dark cycle. After an acclimatization period of one week, the experiment commenced following a thorough observation of the mice's health status. All animal procedures were approved by our institution's Animal Ethics Committee, ensuring compliance with local regulations and ethical standards for animal research.

The mice were randomly divided into four groups: Sham group (undergoing only surgery without SCI), SCI group (undergoing SCI with injection of 10 μl PBS), DSCM group (undergoing SCI with injection of 10 μl DSCM), and DSCM@EVs group (undergoing SCI with injection of 10 μl DSCM@EVs, containing 100 ng DiR-labeled EVs) [13], with 12 mice in each group.

Surgical procedure for constructing the SCI mouse model

Mice were anesthetized by intraperitoneal injection of a mixture of ketamine (70 mg/kg) and xylazine (5 mg/kg). After the cessation of corneal reflexes, the surgical site was shaved and disinfected with povidone-iodine and 70% ethanol. The skin and paraspinal muscle layers of the mouse's back were then incised. A complete transection of a 2 mm segment of the spinal cord at the T9-10 level was achieved by performing a laminectomy. Following the treatment, the paraspinal muscles and skin were sutured in layers, and the area was disinfected with 70% ethanol. Post-surgery, the mice were placed in a warm cage for recovery with access to food and water.

During the 6 weeks post-surgery, in vivo near-infrared fluorescence imaging was conducted weekly on mice in the DSCM@EVs group using the IVIS Spectrum system (Perkin Elmer, with excitation set at 748 nm and emission filter at 780 nm). At week 6, the mice were euthanized. Cardiac perfusion was performed with saline, followed by 4% paraformaldehyde, and major organs, including the spinal cord, heart, liver, spleen, lungs, and kidneys, were collected to assess fluorescence distribution.

After 6 weeks, approximately 2 mm of spinal cord tissue was dissected from the injury site, fixed in 4% paraformaldehyde at 4 °C for 24 h, and then dehydrated overnight in 20% v/v sucrose at 4 °C. This was followed by further dehydration in 30% sucrose at 4 °C for 48 h. The dissected tissues were embedded in OCT and longitudinally sectioned into 10 μm-thick frozen sections using a cryostat (Leica CM1950, Germany). Intact, flat, non-separated, and crease-free frozen sections were selected for histological staining and immunofluorescent co-staining [13, 34].

In the SCI model, regenerative tissue was defined as newly formed structures visible in H&E-stained sections, and cavity volume was measured using image analysis software based on the cross-sectional area in tissue Sect. [36].

Analysis of mouse locomotor behavior and footprints

Weekly assessments were conducted on mice using the Basso-Mouse Scale (BMS). Over a period of 6 weeks post-surgery, hind limb movements of four groups of mice were observed within an 80 cm square grid. The evaluation of hind limb movement capacity was carried out using BMS scores, whereby higher scores reflect the state of recovery of hind limb function following SCI, with scores ranging from 0 (no ankle movement) to 9 (complete functional recovery). Mice with a BMS score higher than 3 on the first day post-injury were excluded.

Weight support and limb coordination abilities were assessed through footprint analysis. The forelimbs and hind limbs of the mice were dyed with blue and red ink, respectively. Subsequently, the mice were allowed to walk freely on a white paper (1 m long, 7 cm wide), with the distance between the hind paw imprints serving as a basis for evaluating weight support, and the distance between the center pad of the forelimb and the center pad of the hind limb used to assess limb coordination. The rotation angle (AR) was defined as the angle formed by two stride lines centered on the third toe and the hind paw [34].

Histological analysis of organ tissues

Spinal cord tissues were sliced and examined for pathological conditions using the H&E staining method. The spinal cord tissues were fixed in 4% paraformaldehyde for 12 h, embedded in paraffin, and then cut into 5 μm sections. The sections were hydrated on glass slides in graded ethanol, stained with H&E, and dehydrated in increasing concentrations of ethanol. Samples were observed under a light microscope at various magnifications. Grey matter alterations and damaged neurons were evaluated using a 6-point scale: (0) no lesions found; (1) 1 to 5 eosinophilic granule neuron cells in the grey matter; (2) 5 to 10 eosinophilic granule neuron cells in the grey matter; (3) over 10 eosinophilic granule neuron cells in the grey matter; (4) small-scale infarction with grey matter damage area less than one-third; (5) moderate-scale infarction with grey matter damage area between half and one-third; (6) severe-scale infarction with grey matter damage area greater than half. The average score of each group of samples was recorded to determine the cumulative score [13, 37].

Adjacent tissue sections were stained with Masson's trichrome staining kit (G1340, Solarbio, China) to detect collagen tissue deposition at the site of injury.

Immunofluorescence co-staining

Tissue slices were permeabilized with 0.5% Triton X-100 in PBS solution and blocked with 5% BSA for 1 h. For cell fixation, 4% paraformaldehyde was applied at room temperature for 15 min, followed by two washes with PBS and permeabilization with 0.5% Triton X-100 (P0096, Beyotime, China) for 10 min. Subsequently, the tissue slices or cells were separately treated with the following primary antibodies: rabbit anti-MAP2 (ab183830, 1:500), rabbit anti-GFAP (ab207165, 1:500), rabbit anti-SYN1 (#5297, 1:200, CST, USA), mouse anti-Nestin (ab81462, 1:100), rabbit anti-SOX2 (ab92494, 1:100), and rabbit anti-F4/F80 (ab6640, 1:200). After overnight incubation at 4 °C, the samples were washed three times with PBS and then incubated with secondary antibodies conjugated with Alexa Fluor 488/594 (A32766/A-21203/A-21206/A32754, 1:500, Thermo Fisher Scientific, USA) for 1 h. Following the incubation, samples were washed three times with PBS and stained with DAPI (10 µL/mL) at room temperature for 10 min. The slices were stored at 4 °C and examined using a confocal microscope (Leica SP8) [13]. All primary antibodies were purchased from Abcam (UK) except for SYN1.

RNA extraction and sequencing

Macrophages incubated with DSCM@EVs were collected before and after incubation, and total RNA was extracted using Trizol reagent (15596026, Invitrogen, Carlsbad, CA, USA). The concentration and purity of RNA samples were determined using a Nanodrop 2000 spectrophotometer (1011U, Thermo Fisher Scientific, USA). Total RNA samples meeting the following criteria were selected for subsequent experiments: RNA Integrity Number (RIN) ≥ 7.0, and 28 S:18 S ratio ≥ 1.5.

The sequencing libraries were generated and sequenced by CapitalBio Technology (Beijing, China). Each sample utilized 5 µg of total RNA. Firstly, Ribo-Zero™ Magnetic Kit (MRZE706, Epicentre Technologies, Madison, WI, USA) was employed to remove ribosomal RNA (rRNA) from total RNA. Subsequently, the NEB Next Ultra RNA Library Prep Kit (#E7775, NEB, USA) was used to construct libraries for Illumina sequencing. Next, the RNA was fragmented into approximately 300 bp (bp) fragments, and the first cDNA strand was synthesized using reverse transcriptase primers and random primers in NEB Next first-strand synthesis reaction buffer (5×). This was followed by second-strand cDNA synthesis in dUTP Mix (10×) second-strand synthesis reaction buffer. The cDNA fragments underwent end repair, polyadenylation, and sequencing adapter ligation. After ligating the Illumina sequencing adapters, the second cDNA strand was digested using the USER enzyme (#M5508, NEB, USA) to construct a strand-specific library. The library DNA was amplified, purified, and subjected to PCR enrichment. Subsequently, the library was assessed using Agilent 2100, and its quantification was performed using the KAPA Library Quantification Kit (KK4844, KAPA Biosystems, USA). Lastly, paired-end sequencing was conducted on the NextSeqCN500 (Illumina, USA) sequencer [38].

Quality control of sequencing data and alignment to the reference genome

The raw sequencing data's quality of paired-end reads was assessed using FastQC software v0.11.8. Preprocessing of the raw data was performed with Cutadapt software version 1.18 to eliminate Illumina sequencing adapters and poly(A) tail sequences. Reads with an N content exceeding 5% were filtered out through a Perl script. The FASTX Toolkit software version 0.0.13 was utilized to extract reads with a base quality of 20 or above, accounting for 70% of the bases. Double-ended sequences were corrected using BBMap software. Lastly, the filtered high-quality reads were aligned to the mouse reference genome using hisat2 software (version 0.7.12) [38].

Differential Gene expression analysis using RNA-seq

In this study, we conducted differential gene expression analysis on the sequencing data using the limma package in R. Differential gene selection was based on criteria where $|\log2FC| > 2$ and P-value < 0.05. Subsequently, heat maps and volcano plots were generated using R to visualize the results.

Functional and gene enrichment analysis of differentially expressed genes in RNA-seq

The differentially expressed genes in the RNA-seq were subjected to Gene Ontology (GO) enrichment analysis and Kyoto Encyclopedia of Genes and Genomes (KEGG) enrichment analysis using the ClusterProfiler package in R. The GO enrichment analysis encompassed analyses of Biological Process (BP), Molecular Function (MF), and Cellular Component (CC), with a significance threshold set at $P < 0.05$.

A gene set related to macrophage polarization pathways was obtained from the Gene Set Enrichment Analysis (GSEA) database (https://www.gsea-msigdb.org/gsea/index.jsp) to perform gene enrichment analysis on the differentially expressed genes in the RNA-seq data, enabling the observation of macrophage polarization patterns.

Machine learning for constructing LASSO regression model to select feature genes

By utilizing the "glmnet" package in R language, a regression analysis was conducted on differentially expressed genes from sequencing data, leading to the identification of the key feature genes associated with M1 macrophage reprogramming [39].

Detection of target gene expression by RT-qPCR

Tissue or cell total RNA was extracted using Trizol reagent (15596026, Invitrogen, USA) following the manufacturer's instructions. The RNA was then reverse-transcribed into cDNA using the PrimeScript RT reagent Kit (RR047A, Takara, Japan). The synthesized cDNA was subjected to RT-qPCR using Fast SYBR Green PCR reagent (11736059, Thermo Fisher Scientific, USA), with each well set up in triplicate. GAPDH was used as the internal reference gene. The relative expression levels were calculated using the $2^{-\Delta\Delta Ct}$ method [40–42] with three experimental replicates. The primer sequences synthesized by Takara are provided in Table S2.

Detection of target protein expression by western blot

The Pierce BCA Protein Assay Kit (23227, Thermo Fisher Scientific, USA) was used to quantify cell protein samples isolated from tissue and whole cell lysates. Proteins from tissues and cells were extracted using RIPA buffer. From each sample, 20 μg of protein was loaded onto a 10% SDS-PAGE gel and electrophoresed at 100 V for 90 min. After electrophoresis, the proteins were transferred onto a membrane for 1 h. The uccessful transfer was verified using Ponceau S staining at room temperature for 30 min. Once protein transfer was confirmed, the membrane was blocked with 5% nonfat milk for 1 h and then incubated overnight at 4 °C with the following primary antibodies from Abcam (Cambridge, UK): mouse anti-HSP70 (ab2787, 78 kDa, 1:1000), rabbit anti-CD9 (ab307085, 23 kDa, 1:1000), rabbit anti-CD81 (ab109201, 26 kDa, 1:1000), rabbit anti-MAP2 (ab32454, 199 kDa, 1:1000), rabbit anti-GFAP (ab7260, 55 kDa, 1:10000), rabbit anti-SYN1 (ab254349, 75 kDa, 1:1000), rabbit anti-COL1 (ab138492, 139 kDa, 1:1000), rabbit anti-LAMA1 (ab315275, 338 kDa, 1:1000), rabbit anti-LAMB1 (DF3618, 197 kDa, 1:1000), mouse anti-TNC (MA5-16086, 231 kDa, 1:1000), mouse anti-FGF2 (MA5-15276, 17 kDa, 1:1000), mouse anti-GAPDH (ab8245, 37 kDa, 1:1000), and rabbit anti-Calnexin (ab133615, 68 kDa, 1:1000).

The next day, secondary antibody incubation was performed using either Peroxidase-conjugated AffiniPure Goat Anti-Rabbit IgG (H + L) (#111035003, Jackson ImmunoResearch, USA) or Peroxidase-conjugated AffiniPure Goat Anti-Mouse IgG (H + L) (#115035003, Jackson ImmunoResearch, USA) at room temperature for 1 h. After washing the membrane three times with TPBS, an enhanced chemiluminescence reagent (WP20005, Thermo Fisher Scientific, USA) was applied to visualize the immunoreactive bands, and images were captured using the ChemiDoc XRS Plus luminescent image analyzer (Bio-Rad Laboratories, Hercules, CA, USA). Band intensity for each group was quantified using Image J software, with GAPDH used as the internal control [43]. Experiments were repeated three times.

Statistical analysis

In our study, we performed statistical analyses on the research data using the SPSS software package (version 23.0, IBM SPSS) or GraphPad Prism software (version 8.0). Descriptive statistics were presented as means ± standard deviations for continuous variables. Initially, normality and homogeneity of variance were assessed. For data groups meeting the criteria of normal distribution and equal variance, we applied independent sample t-tests. Multiple group comparisons were conducted using one-way analysis of variance or repeated measures analysis of variance. Pearson's correlation analysis was utilized to assess the relationship between two variables. Statistical significance was indicated by $P < 0.05$, $P < 0.01$, and $P < 0.001$.

Results

Successful preparation of DSCM@EVs

Currently, in clinical practice, complete SCI remains incurable [44]. A decellularized tissue matrix (DSCM) is a commonly used natural biomaterial for soft tissue repair or regenerative therapy. For instance, DSCM hydrogels can serve as carriers to deliver cells, growth factors, or genes to the diseased injury site, promoting the therapeutic process [13]. Moreover, DSCM@EVs have been reported to facilitate spinal cord repair in SCI processes [45]. In this study, we, for the first time, loaded EVs from MSCs onto DSCM derived from the spinal cord, termed DSCM, to obtain functionalized DSCM@EVs, aiming to investigate their reparative effects on SCI and potential regulatory mechanisms.

First, mouse MSCs were characterized. Flow cytometry revealed positive expression of CD90, CD73, CD105, and CD44, and negative expression of CD45 and CD31 in MSCs (Figure S1A). In addition, MSCs were induced to differentiate into adipogenic, osteogenic, and chondrogenic lineages, confirming their multipotent differentiation potential (Figure S1B). EVs derived from MSCs were then obtained through differential centrifugation and morphologically characterized by TEM, showing that MSC-EVs had a uniform, spherical or oval membranous vesicle structure (Figure S1C). NTA results indicated an average EV particle size of approximately 120 nm, an ideal size (100–150 nm) for efficient cellular uptake by

DSCM@EVs (Figure S1D). Western blot analysis demonstrated high expression of EV-specific surface markers CD9, HSP70, and CD81, with no expression of Calnexin, confirming the successful isolation of EVs (Figure S1E).

Next, DSCM was obtained from miniature pig spinal cords, and H&E staining was used to compare the nuclear signals between NSCM (native spinal cord matrix) and DSCM. Results indicated the complete absence of nuclear signals in the DSCM group (Figure S1F). Furthermore, residual DNA quantification showed a reduction of over 98% in DSCM compared to NSCM, with residual DNA levels < 50 ng/mg ECM (Figure S1G), indicating successful decellularization. Quantitative analysis of collagen and sGAG in DSCM and DNM revealed that collagen (DSCM: 659.59 μg/mg vs. DNM: 860.95 μg/mg, $n = 3$, $P < 0.5$) and sGAG concentrations (DSCM: 4.26 vs. DNM: 6.59 μg/mg) were slightly lower in DSCM than in DNM (Figure S1H). Western blot analysis further confirmed significant expression of collagen, tenascin family (TNC), fibroblast growth factor (FGF2), and laminin in DSCM, which are known to promote NSC proliferation and differentiation, thereby regulating inflammation and tissue repair [13] (Figure S1I). SEM observation of gelled DSCM showed a nanofibrous structure (Figure S1J), with a porosity and fiber diameter of 43.4% and 86.7 nm, respectively, indicating the capacity of DSCM to load more EVs (Figure S1K).

Finally, DiR-labeled EVs were dissolved in DSCM solution to prepare DSCM@EVs (1 μg/μL). Fluorescence confocal microscopy showed that labeled EVs displayed good monodispersity within DSCMs, with fluorescence intensity in the hydrogel increasing as EV concentration increased (Fig. 1A), confirming successful EV loading into DSCM. To further evaluate the impact of DSCM on EV activity, DSCM@EVs were dissolved in PBS at 37 °C to monitor EV release, showing sustained EV release over 14 days, reaching 99% at 37 °C (Fig. 1B). Additionally, particle size and morphology of released EVs in PBS were examined, indicating an average particle size of approximately 120 nm with intact vesicular structure. Released EVs consistently expressed positive EV markers CD9, HSP70, and CD81, with no expression of the negative marker Calnexin, consistent with freshly isolated EVs, demonstrating that DSCM maintained EV structural integrity (Fig. 1C-E). Rheological and mechanical properties of gelled DSCM were assessed, showing favorable gelation time and storage modulus, indicating good gelation performance (Figure S1L).

These results confirm the successful extraction of MSC-derived EVs, their loading into spinal cord-derived DSCM hydrogel, and the preparation of DSCM@EVs. These DSCM@EVs were capable of sustained EV release in vitro while preserving EV structural integrity.

DSCM@EVs promote NSC differentiation into neurons and suppress astrocyte formation to alleviate SCI

To further verify the potential of DSCM-loaded EVs in alleviating SCI, we established an SCI mouse model and administered drug injections at the injury site to observe the recovery of motor function in each group of mice. Using near-infrared fluorescence imaging, we observed the in vivo release of EVs and found that on postoperative

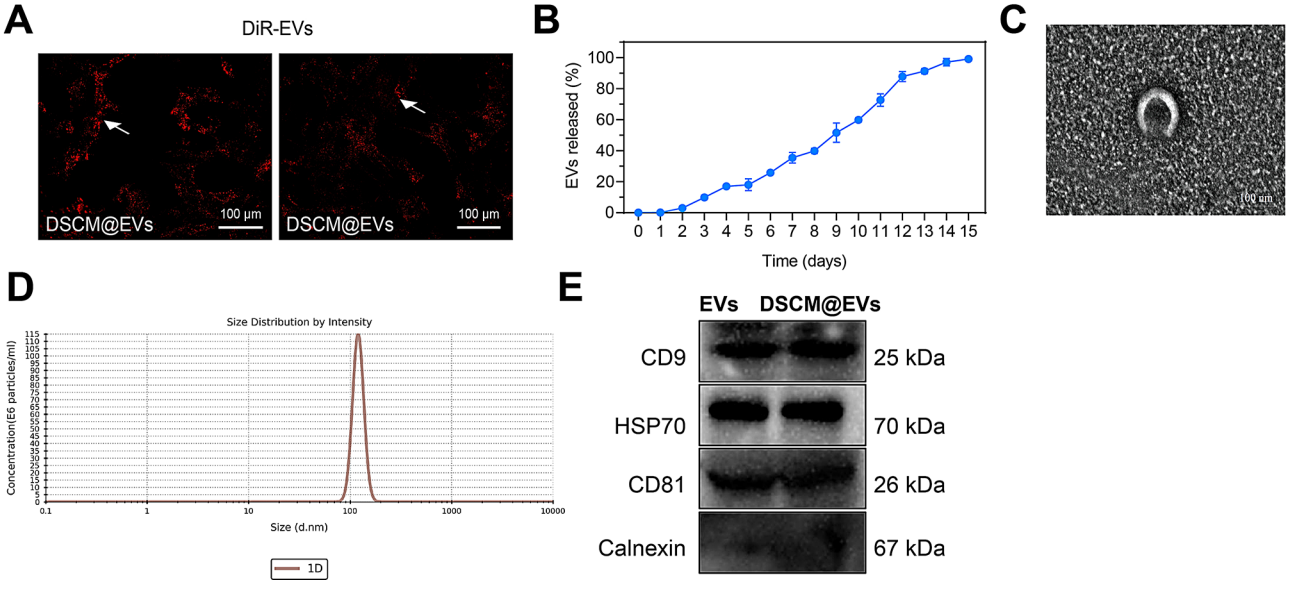

Fig. 1 Characterization of DSCM@EVs. Note: (**A**) Fluorescence confocal microscopy observation of the distribution of EVs in DSCM@EVs, with red DiR-labeled EVs. Scale bar = 100 μm; (**B**) EVs release assay from DSCM@EVs; (**C**) Transmission electron microscopy observation of the morphology of EVs released from DSCM@EVs. Scale bar = 100 nm; (**D**) Nanoparticle tracking analysis of the size of EVs released from DSCM@EVs; (**E**) Western blot analysis of the expression of marker proteins in EVs released from DSCM@EVs. Cell experiments were repeated at least three times

day 42, mice in the DSCM@EVs group still exhibited DiR fluorescence signals at the SCI site. This finding indicates that DSCM exhibits strong adhesion to tissues, effectively securing EVs at the SCI site and facilitating their sustained and controlled release (Fig. 2A-B). Furthermore, fluorescence observations of major organs collected on day 42 revealed a widespread distribution of fluorescence in the SCI area and kidney regions (Fig. 2C), providing additional evidence of DSCM's binding effect on EVs.

Motor behavior of the mice was assessed using the Basso-Mouse Scale, with Fig. 2D illustrating that all groups displayed normal movement before the injury, which significantly declined after SCI surgery. Following treatment with DSCM and DSCM@EVs, there was some recovery in the mice's motor abilities, with the DSCM@EVs group showing the best recovery. Additionally, based on the distribution of footprints (Fig. 2E) and the evaluation of the support base (Fig. 2F), stride length (Fig. 2G), rotation angle (Fig. 2H), and toe drag measurements

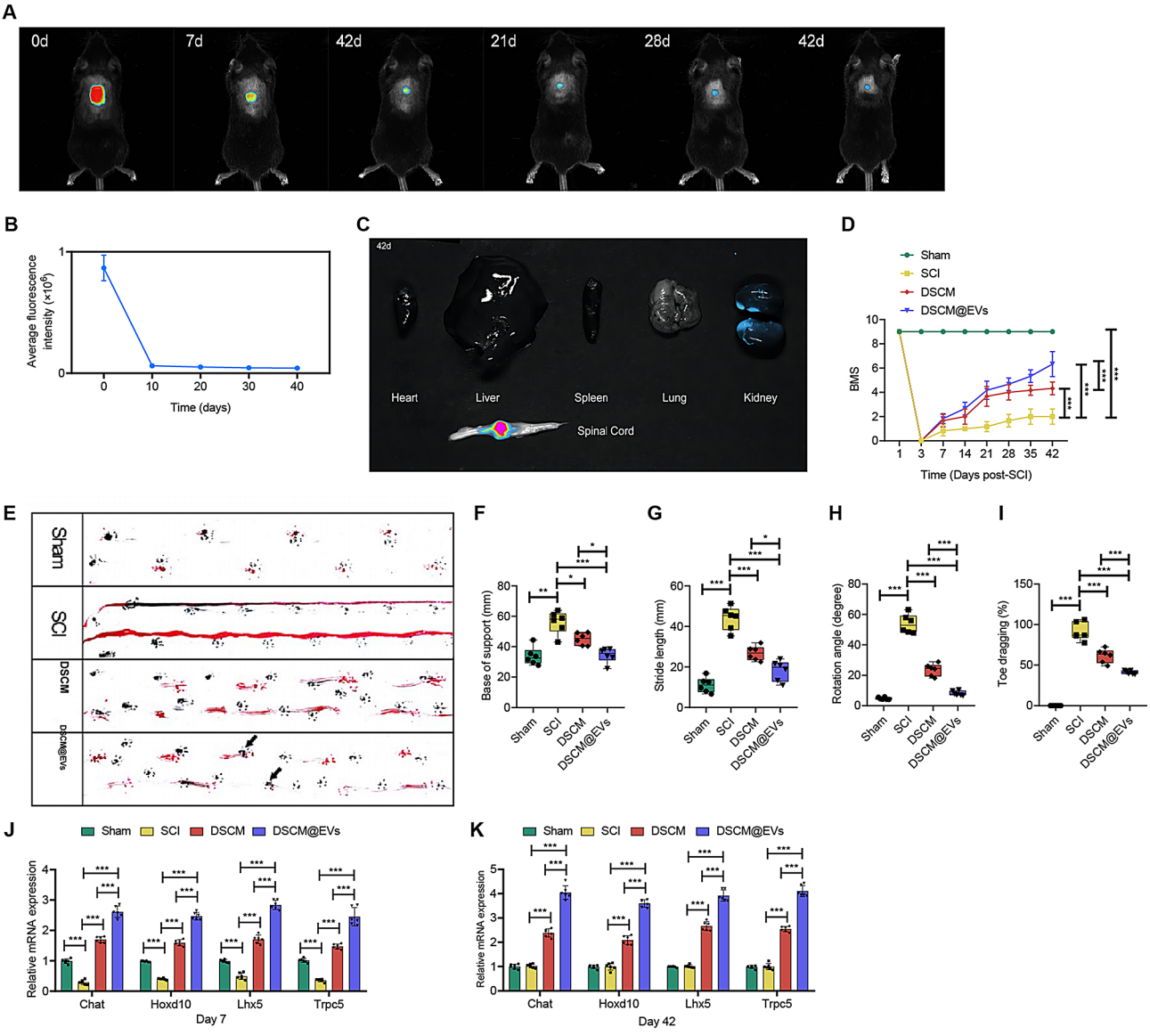

Fig. 2 In Vivo Release of DSCM@EVs and Their Effect on The Motor Function of Mice. Note: (**A**-**B**) Near-infrared fluorescence observation of the fluorescence intensity and quantitative fluorescence image at the spinal cord of mice in the DSCM@EVs group; (**C**) Fluorescence images of major organs of mice in the DSCM@EVs group on day 42 post-administration; (**D**) Evaluation of motor function of mice in each group using Basso Mouse Scale (BMS) scoring on day 42; (**E**) Footprint distribution of mice in each group on day 42; (**F**-**I**) Support, rotation angle, step length, and toe drag distance of mice in each group on day 42; (**J**) Gene expression levels of tissue regeneration-related factors in mice of different groups at the subacute phase (7 days) detected by RT-qPCR; (**K**) Gene expression levels of tissue regeneration-related factors in mice of different groups at the chronic phase (42 days) detected by RT-qPCR. Six mice per group, * indicates a significant difference between the two groups, $P < 0.05$, ** $P < 0.01$, *** $P < 0.001$

(Fig. 2I), the coordination of the mice's limbs was assessed, showing a consistent trend with Fig. 2D and indicating a significant improvement in limb coordination with DSCM@EVs treatment.

Moreover, we examined the effects of DSCM@EVs on the expression of Regeneration-Associated Genes (RAGs) during the subacute (postoperative day 7) and chronic SCI (postoperative day 42) processes. These genes were selected from the categories of nervous system development (GO: 0007399), motor recovery (GO: 0007626), and chemical synaptic transmission (GO: 0007268) [46]. RT-qPCR results showed a significant decrease in the expression of RAGs in spinal cord tissue during the subacute phase post-SCI, which significantly increased after treatment with DSCM and DSCM@EVs, both in the subacute and chronic phases compared to the SCI group, with the DSCM@EVs group showing a more significant increase than the DSCM group (Fig. 2J-K).

At 6 weeks postoperatively, spinal cord tissues were harvested (Fig. 3A1-A4), and H&E staining revealed that compared to the Sham group, SCI mice exhibited minimal regenerative tissue and increased cavity volume in the spinal cord tissue. However, after treatment with DSCM and DSCM@EVs, the spinal cord of mice displayed a linear and ordered structure of regenerative tissue, reduced cavity volume, and significantly lower injury scores, with the most notable changes observed in the DSCM@EVs group (Fig. 3B1-B4, D). This indicates that DSCM@EVs notably promoted spinal cord tissue regeneration. Additionally, Masson's trichrome staining demonstrated a significant increase in blue collagen deposition in spinal cord tissue post-SCI, which significantly decreased after DSCM and DSCM@EVs treatments, with the lowest levels observed in the DSCM@EVs group (Fig. 3C1-C4, E), suggesting that DSCM@EVs significantly reduced collagen deposition, creating a suitable microenvironment for axonal regeneration.

Finally, immunofluorescence co-staining was performed to evaluate the differentiation of NSCs in the SCI area. As shown in Fig. 3F, although MAP2-positive neurons and GFAP-positive astrocytes were present in the injury sites of mice in the SCI, DSCM, and DSCM@EVs groups, the DSCM@EVs group exhibited the highest density of positive signals for neurons and the lowest for GFAP-positive astrocytes in the transverse section, followed by the DSCM group (Fig. 3F). Additionally, Western blot analysis of MAP2 and GFAP expression in spinal cord tissue further confirmed the results of immunofluorescence co-staining (Fig. 3G).

In summary, these findings suggest that DSCM can slowly release EVs in vivo, and after loading with DSCM, it can further enhance spinal cord repair in SCI mice, likely by promoting the differentiation of NSCs into neurons rather than astrocytes.

Significant increase in infiltration of M1 macrophages in SCI Revealed by Bioinformatics Analysis of Public Database

SCI leads to a rapid inflammatory response, in which immune cells swiftly infiltrate the injured area and secrete pro-inflammatory cytokines. This results in neuronal death, demyelination of axons, and functional deficits [46]. Previous studies have shown that DSCM can recruit NSCs to the injury site to promote SCI repair [13]; however, the relationship between DSCM and immune cell infiltration has not been investigated. Therefore, we downloaded SCI-related microarray data from the GEO database to delve deeper into immune cell infiltration in SCI.

Initially, we merged two SCI microarray datasets, GSE5296 and GSE47681, and performed batch correction. Figure S2 illustrates that prior to batch correction, there were significant differences between these two datasets, which were markedly reduced and noise minimized after batch correction.

Subsequently, we employed the CIBERSORT algorithm to estimate immune cell infiltration in the merged dataset. By generating heatmaps and bar graphs of 22 types of immune cell infiltrates, we observed a heightened level of immune cell infiltration in SCI spinal cord tissue. Specifically, the infiltration proportions of monocytes, dendritic cells, and M1 macrophages significantly increased (Fig. 4A-B), with correlations existing among these cell types (Fig. 4C). Furthermore, the PCA analysis results in Fig. 4D demonstrate that SCI diseases can be distinguished based on the degree of immune cell infiltration.

Furthermore, we utilized WGCNA to construct a co-expression network and identify core genes significantly associated with immune infiltration phenotypes in SCI. Analyzing the batch-corrected merged dataset of GSE5296 and GSE47681, we selected a soft-thresholding parameter β of 3 when the correlation coefficient threshold was set at 0.9 (Fig. 5A). Subsequently, we established ten co-expression modules through WGCNA analysis (Fig. 5B). Module trait correlation analysis revealed a significant negative correlation between monocytes and the turquoise and brown modules, while dendritic cells and M1 macrophages showed a significant positive correlation with the red module's core genes (Fig. 5C-D).

Previous studies have indicated that M1 macrophages inhibit NSC differentiation by secreting pro-inflammatory factors, thereby impeding SCI treatment progress [47]. Therefore, we speculate that after loading DSCM-derived EVs, modulation of M1 macrophages could potentially reduce the inflammatory environment in the injury site, consequently promoting NSC differentiation. As a result, our future research will focus on macrophages and conduct further analysis using core genes from the red module significantly associated with M1 macrophages, as depicted in Fig. 5D.

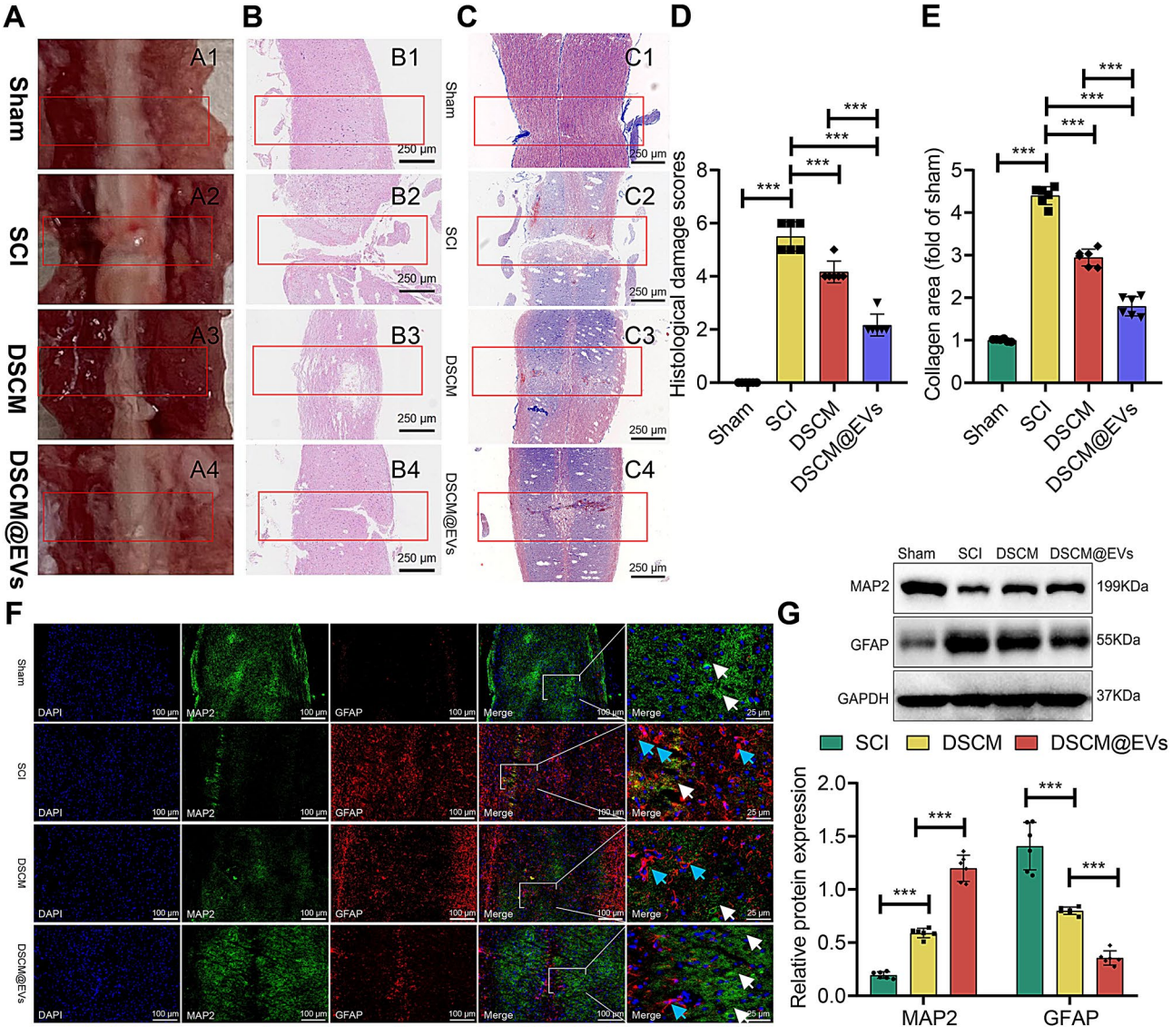

Fig. 3 Influence of DSCM@EVs on Spinal Cord Tissue Healing, Collagen Deposition, and NSCs Differentiation in Mice. Note: (**A**) Bright-field images of spinal cord or injury sites in each group of mice; (**B**) H&E staining to assess spinal cord tissue regeneration in each group of mice, with a scale bar of 250 μm; (**C**) Masson staining to evaluate collagen deposition in spinal cord tissue of each group of mice, with a scale bar of 250 μm; (**D**) SCI scores in Figure B; (**E**) Collagen area in Figure C; (**F**) Immunofluorescent co-staining to detect the expression of MAP2 (White arrows) and GFAP (Red arrows) in spinal cord tissue of each group of mice, with a scale bar of 100 μm; (**G**) Western blot analysis to assess the protein expression levels of MAP2 and GFAP in spinal cord tissue of each group of mice; * indicates comparison between two groups, $P < 0.05$, ** $P < 0.01$

DSCM@EVs induce M1 macrophage reprogramming towards M2 macrophages in vivo and in Vitro

Macrophages can be activated into M1 and M2 phenotypes under different conditions. M1 macrophages primarily secrete pro-inflammatory factors and play a crucial role in the early stages of inflammation, while M2 macrophages can inhibit inflammatory factors, suppress inflammatory responses, and promote tissue repair [48].

In order to investigate whether DSCM@EVs affect macrophage infiltration in the injury site, we divided experimental mice into Sham, SCI, DSCM, and DSCM@EVs groups. By performing RT-qPCR analysis on spinal cord tissues of mice to evaluate macrophage infiltration at the injury site, the results showed that post-SCI surgery, the expression of M1 macrophage markers Nos2, Ccr7, and Cd86 significantly increased. Following treatment with DSCM and DSCM@EVs, the expression of M1 macrophage markers significantly decreased, while the expression of M2 macrophage markers Arg1, Cd206, and Il-10 significantly increased. The therapeutic effect of DSCM@EVs was more pronounced (Fig. 6A-B).

Furthermore, we conducted immunofluorescence co-staining on spinal cord tissues of mice from the SCI and DSCM@EVs groups. F4/80 + represented total

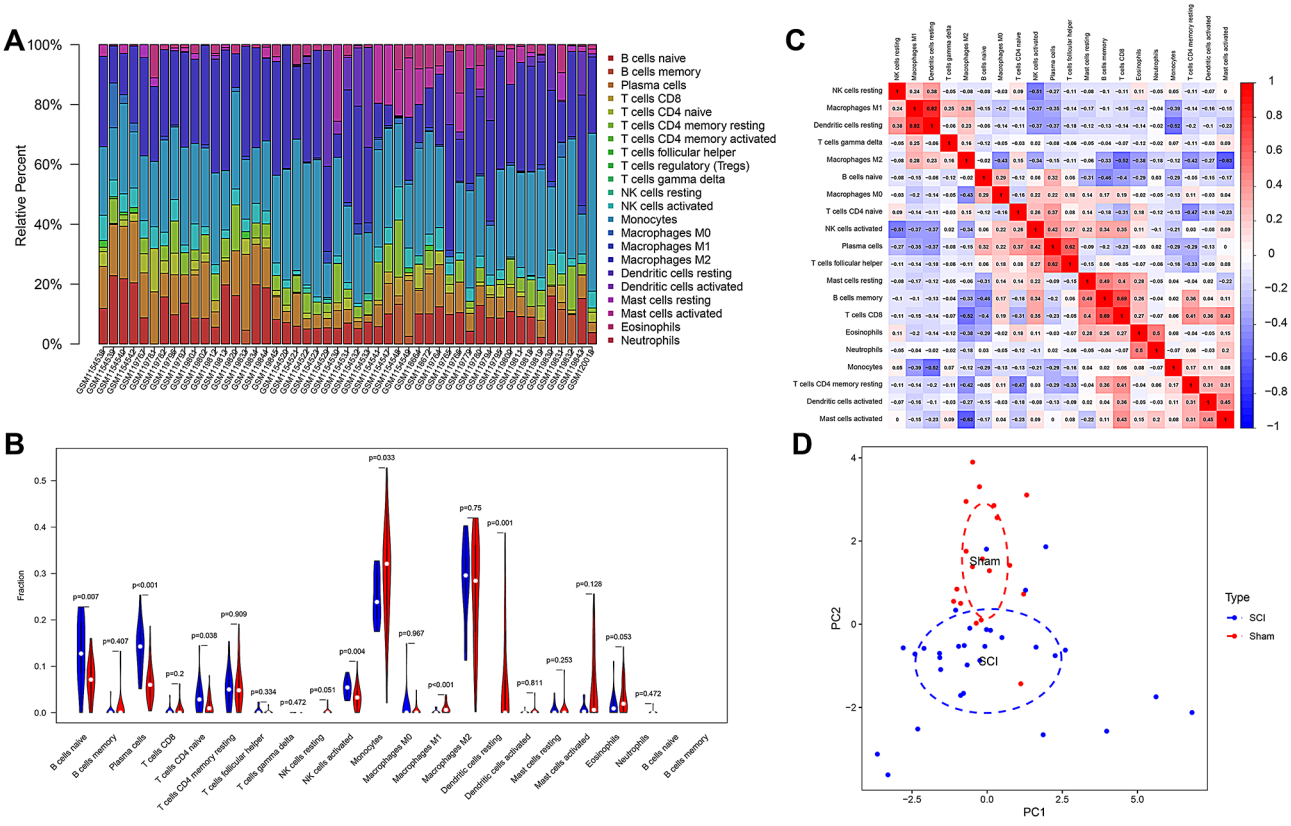

Fig. 4 Immunocyte Infiltration in SCI Analyzed Through Bioinformatics Methods. Note: (**A**) Bar graph displaying the proportions of 22 types of immune cell infiltration in the combined dataset of GSE5296 and GSE47681, analyzed using the CIBERSORT algorithm; (**B**) Violin plot illustrating the proportions of 22 types of immune cell infiltration in the combined dataset of GSE5296 and GSE47681, with the Sham group shown in blue and the SCI group in red, analyzed using the CIBERSORT algorithm; (**C**) Correlation heatmap showing the proportions of immune cell infiltration in the combined dataset of GSE5296 and GSE47681, analyzed using the CIBERSORT algorithm; (**D**) PCA of immune cell infiltration dispersion in the SCI and Sham groups in the combined dataset of GSE5296 and GSE47681. SCI: 31 cases, Sham: 18 cases

macrophages, and CD206 + symbolized M2 macrophages. The results indicated that compared to day 7, both total macrophages and M2 macrophages significantly decreased on day 42, suggesting gradual tissue repair in the spinal cord. Whether on day 7 or day 42 post-SCI surgery, there was no change in total macrophages in the spinal cord of SCI mice before and after treatment with DSCM and DSCM@EVs, while M2 macrophages significantly increased. The therapeutic effect of DSCM@EVs was more pronounced (Fig. 6C-G). This suggests that DSCM@EVs might induce the transformation of M1 macrophages into M2 macrophages.

Further cell verification was conducted in vitro. Mouse bone marrow macrophages were first induced into M1 macrophages, followed by co-incubation of DSCM@EVs with M1 macrophages and NSCs. On the 3rd day, live/dead cell staining revealed that DSCM@EVs had no cytotoxic effects on the cells (Figure S3D-F). Subsequently, DSCM@EVs were co-incubated with bone marrow macrophages, and at different time points during IFN-γ/LPS-induced M1 macrophage polarization, RT-qPCR results showed that in the process of inducing bone marrow macrophages towards M1 phenotype, the expression levels of M1 macrophage markers significantly decreased in the DSCM@EVs treatment group, while the expression levels of M2 macrophage markers significantly increased (Fig. 6H-I).

DSCM@EVs induce M1 macrophage reprogramming to accelerate NSCs differentiation

In the subsequent study, we further investigated the impact of DSCM@EVs on the functional alterations of NSCs following M1 macrophage reprogramming. M1 macrophages were either cultured alone or co-treated with DSCM@EVs, and the corresponding CM was collected. Subsequently, the CM was added to the NSCs culture medium to observe the changes in NSCs functionality.

Initially, NSCs were isolated from mouse spinal cord tissues and expanded to the third passage (P3). Immunofluorescent co-staining results revealed that over 90% of NSCs were positive for NESTIN, and over 95% were positive for SOX2 (Figure S3A-C). Moreover, live/dead cell staining (Figure S3D-F) showed that co-culturing

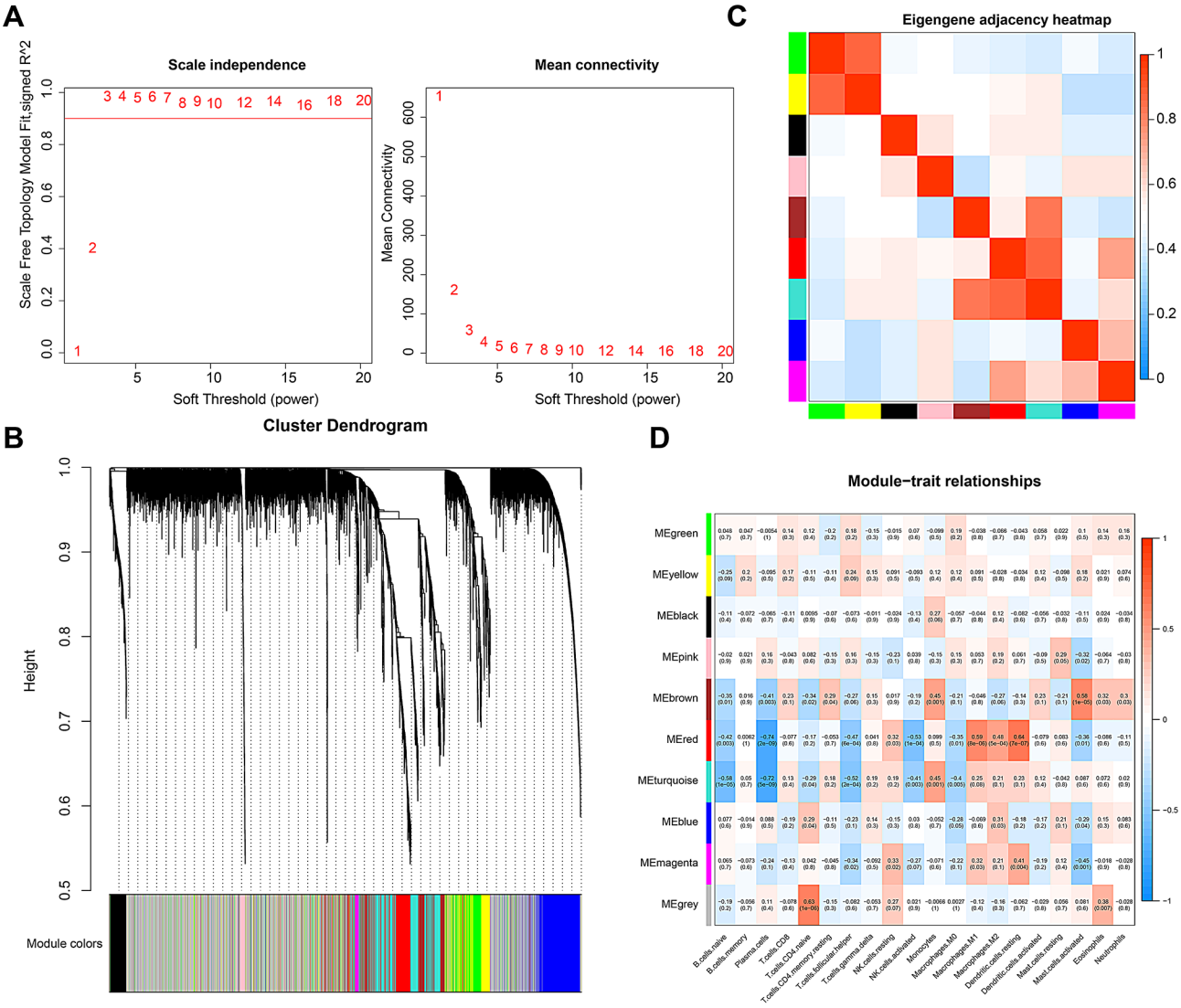

Fig. 5 Construction of Gene Co-expression Network and Module Feature Correlation Analysis. Note: (**A**) Analysis of scale-free fitting indices and average connectivity of various soft-threshold powers; (**B**) Gene co-expression network constructed by WGCNA, where each color represents a module within the network; (**C**) Analysis of inter-module correlations; (**D**) Heatmap depicting the correlations between different modules and immune cells, with each cell containing the correlation coefficient and the corresponding p-value

DSCM@EVs with NSCs had no cytotoxic effects on NSCs after three days of incubation.

NSCs proliferation and migration were assessed through CCK-8, EdU staining, and migration experiments. The results indicated that the CM derived from M1 macrophages treated with DSCM@EVs significantly enhanced NSCs proliferation and migration compared to CM from M1 macrophages alone (Fig. 7A-C). Further evaluation through immunofluorescent co-staining and RT-qPCR analysis of neuron (MAP2) and astrocyte (GFAP) markers showed a significant promotion of NSCs differentiation into neurons (increased MAP2 expression) rather than astrocytes (decreased GFAP expression) after co-culture with DSCM@EVs and M1 macrophages (Fig. 7D-F). Additionally, morphological observation of each group of cells showed that newly generated neurons in the group co-cultured with DSCM@EVs and M1 macrophages displayed a polygonal shape with several elongated projections and more complex dendritic branching (Figure S4B) [49]. Lastly, positive expression of the neuronal axon marker SYN1 [50] confirmed that co-culturing DSCM@EVs with M1 macrophages promoted neuronal axon formation (Fig. 7G).

To directly demonstrate that M2 macrophages promote NSCs proliferation, migration, neuronal differentiation, and axon formation, we co-cultured NSCs with bone marrow-derived macrophages (M0), polarized M1 and M2 macrophage CM. The results confirmed that only M2 macrophages, and not M0 or M1 macrophages, could

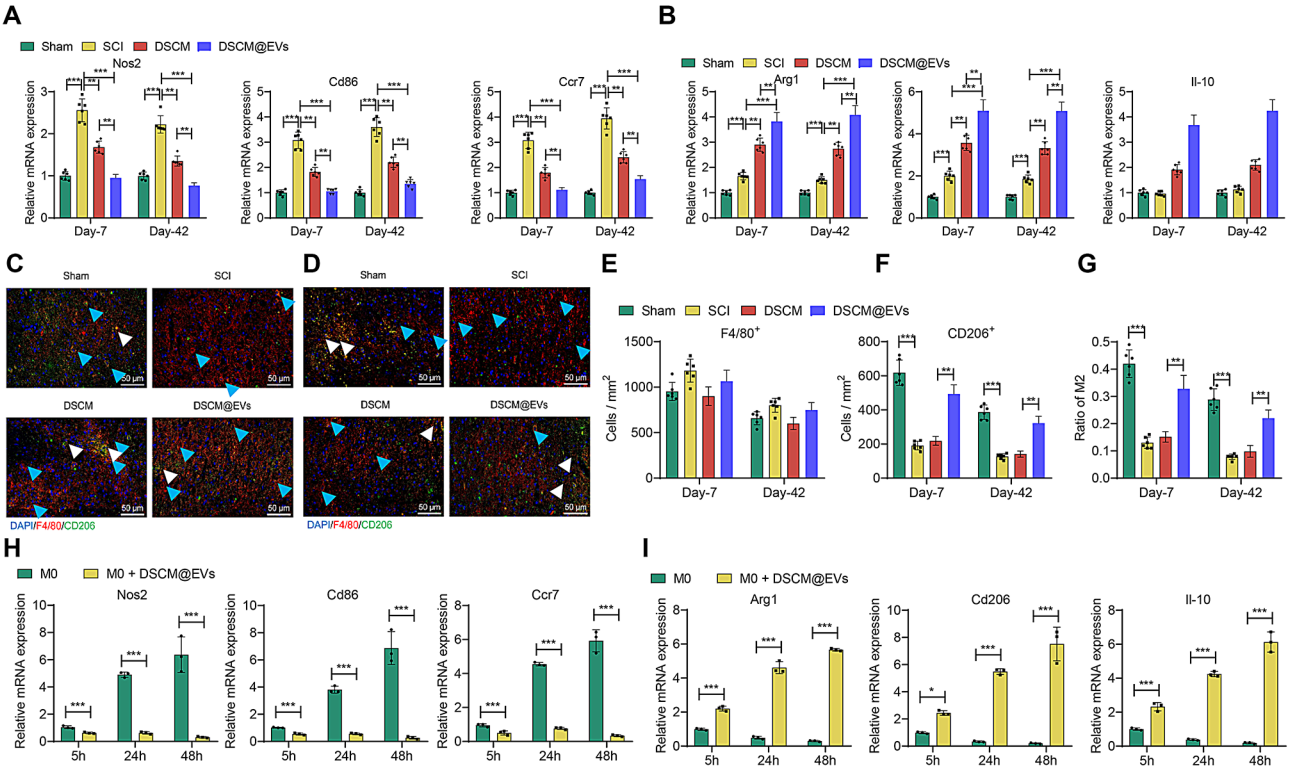

Fig. 6 Impact of DSCM@EVs on Reprogramming of M1-Type Macrophages. Note: (**A**-**B**) RT-qPCR was used to assess the gene expression levels of M1 macrophage markers Nos2, Ccr7, and Cd86, as well as M2 macrophage markers Arg1, Cd206, and Il-10 in the spinal cord tissues of mice in each group; (**C**-**D**) Immunofluorescence double staining was performed on spinal cord tissues of mice from each group on Day 7 and Day 42 post-SCI. The staining visualized the infiltration of total macrophages and M2 macrophages, with DAPI staining the nuclei in blue, F4/80 staining total macrophages in green (Blue arrows), CD206 staining M2 macrophages in red (White arrows), scale bar = 50 μm; (**E**) Total macrophage count in Figures C-D; (**F**) M2 macrophage count in Figures C-D; (**G**) Proportion of M2 macrophages to total macrophages in Figures C-D; (**H**-**I**) RT-qPCR analysis was conducted to measure the gene expression levels of M1 macrophage markers Nos2, Ccr7, and Cd86, as well as M2 macrophage markers Arg1, Cd206, and Il-10 in macrophages from each group. Each group consisted of 6 mice, * indicates a comparison between two groups, $P < 0.05$, ** $P < 0.01$, *** $P < 0.001$. Cell experiments were repeated at least three times

enhance NSCs proliferation, migration, neuronal differentiation, and axon formation (Figure S4).

These findings collectively demonstrate that DSCM@EVs can induce M1 macrophage reprogramming towards the M2 phenotype, reduce the inflammatory microenvironment in SCI, and promote NSCs proliferation, migration, neuronal differentiation, and axon formation.

Identification of key factor Slamf9 in DSCM@EVs regulating M1 macrophage reprogramming through RNA-seq combined with machine Algorithm Screening

To investigate further how DSCM@EVs regulate the reprogramming of M1 macrophages, we co-cultured M1 macrophages with or without DSCM@EVs and subsequently performed RNA-seq analysis on the M1 macrophages before and after culturing, aiming to identify key regulatory factors.

Initially, we conducted standardization processing on the sequencing data (Figure S5A-B) and then performed differential gene expression analysis, identifying a total of 120 differentially expressed genes, with 7 genes upregulated and 113 genes downregulated (Figure S5C-D). Subsequently, we subjected the differentially expressed genes to Gene Ontology (GO) analysis, revealing enrichment of these genes in Biological Processes (BP), including leukocyte migration, leukocyte chemotaxis, and acute inflammatory response, Cellular Components (CC) such as membrane raft, membrane microdomain, and apical part of cell, and Molecular Functions (MF) like cytokine activity, cytokine receptor binding, and G protein-coupled receptor binding (Figure S6A). The Kyoto Encyclopedia of Genes and Genomes (KEGG) analysis showed that these differentially expressed genes were mainly enriched in signaling pathways such as Arginine biosynthesis, Cytokine-cytokine receptor interaction, HIF-1 signaling pathway, IL-17 signaling pathway, and TNF signaling pathway (Figure S6B), which are associated with inflammation and consistent with our previous laboratory and in vitro study findings. Furthermore, through Gene Set Enrichment Analysis (GSEA), we demonstrated that the gene enrichment of M2 macrophages significantly increased after

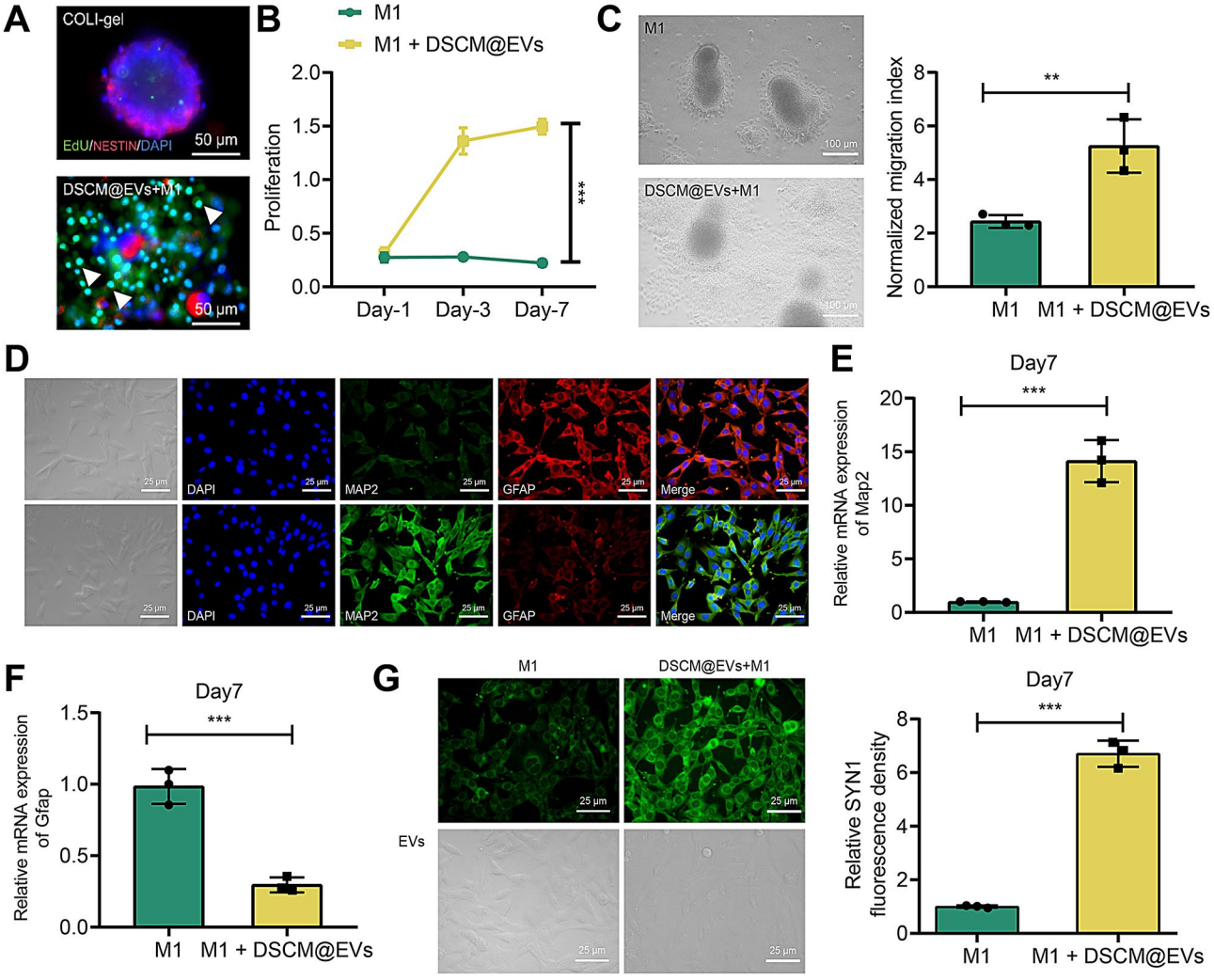

Fig. 7 Impact of DSCM@EVs on NSCs Differentiation. Note: NSCs were cultured with conditioned media obtained by co-incubating M1-type macrophages with or without DSCM@EVs. (**A**) EdU staining was performed to assess NSCs proliferation in each group, where blue represents DAPI-stained nuclei, red represents NESTIN-stained NSCs, and green represents EdU-stained proliferating NSCs (White arrows), depicted with a scale bar of 50 μm. (**B**) A CCK-8 assay was conducted to evaluate the proliferation of NSCs in each group. (**C**) The migration of NSCs in each group was examined; for better visualization of the migration distance differences. (**D**) Immunofluorescence co-staining was carried out to detect the expression of neuronal and glial cell markers in NSCs of each group, with a scale bar of 25 μm. (**E**-**F**) RT-qPCR was utilized to measure the gene expression levels of neuronal and glial cell markers in NSCs of each group. (**G**) Immunofluorescence co-staining was performed to assess neuronal axon formation in NSCs of each group, with a scale bar of 25 μm. * denotes statistical significance between the two groups, $P < 0.05$; cell experiments were repeated at least three times

co-cultivation with M1 macrophages and DSCM@EVs (Figure S6C).

To further identify key factors, we employed machine learning to construct a LASSO regression model for the analysis of differentially expressed genes, ultimately obtaining 4 core genes: Slamf9, Nos2, Eno2, and Egln3 (Fig. 8A-B). Subsequently, we merged the datasets of GSE5296 and GSE47681 with 277 core genes significantly associated with M1 and M2 macrophages (Fig. 5D) as well as 6417 differentially expressed genes, followed by intersection operations with the core genes from LASSO regression and RNA-seq differentially expressed genes, resulting in the unique key gene: Slamf9 (Fig. 8C). We then analyzed the expression of Slamf9 in the RNA-seq and GEO merged datasets. The results revealed that after co-cultivation of M1 macrophages with DSCM@EVs, Slamf9 expression significantly decreased in RNA-seq data (Fig. 8D); in the GEO merged dataset, Slamf9 expression was significantly increased in the SCI group compared to the Sham group, and it was positively correlated with the infiltration of M1 macrophages (Fig. 8E-F). Prior studies indicate that Signaling lymphocyte activation molecule family member 9 (SLAMF9) is a cell surface protein of the leukocyte surface receptor CD2/SLAM family involved in the regulation of immune response and inflammatory processes [51, 52].

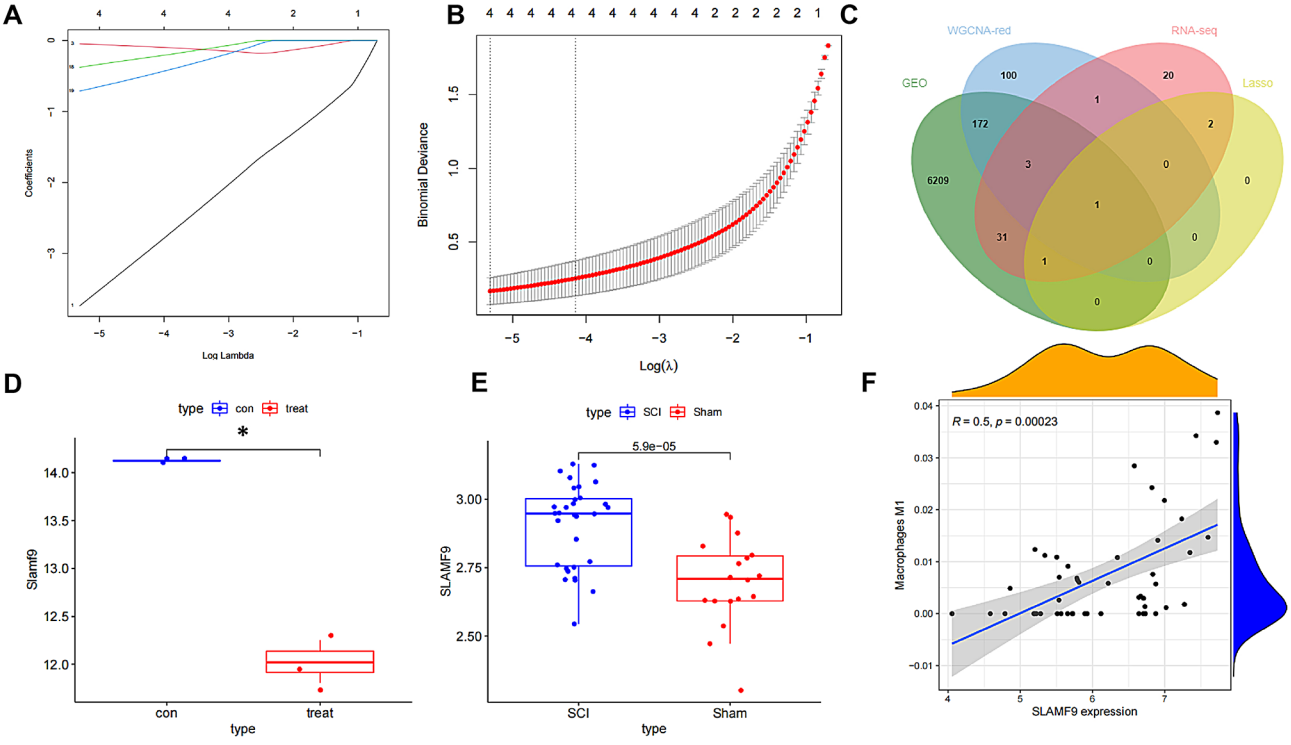

Fig. 8 Key Factors Regulating Reprogramming of M1 Macrophages by DSCM@EVs. Note: (**A**) Path diagram of LASSO coefficient for differentially expressed genes in RNA-seq; (**B**) Cross-validation curve for differentially expressed genes in RNA-seq; (**C**) Venn diagram showing intersection of LASSO genes, GEO merged data, differentially expressed genes, core genes of M1-M2 macrophages, and differentially expressed genes in RNA-seq; (**D**) Bar chart of Slamf9 expression in RNA-seq, where the con group represents M1 macrophages and the treat group represents M1 macrophages treated with DSCM@EVs; (**E**) Bar chart of Slamf9 expression in GEO merged dataset; (**F**) Analysis of correlation between Slamf9 in GEO merged dataset and infiltration of M1 macrophages

In conclusion, we hypothesize that Slamf9 might be a key gene in the reprogramming of M1 macrophages to M2 induced by DSCM@EVs.

DSCM@EVs suppress Slamf9 expression to promote M1 macrophage reprogramming, accelerating NSCs differentiation

Through bioinformatics analysis, we identified that DSCM@EVs modulate the critical factor Slamf9 in M1 macrophage reprogramming. RT-qPCR results demonstrated a significant increase in Slamf9 expression in the spinal cord tissue of mice post-SCI surgery. However, compared to the DSCM group, treatment with DSCM@EVs resulted in a notable decrease in Slamf9 expression in the spinal cord tissue of mice (Fig. 9A). Co-culturing M1 macrophages with DSCM@EVs significantly lowered the expression levels of Slamf9 (Fig. 9B). Further co-culturing DSCM@EVs with M1 macrophages overexpressing or lacking Slamf9 revealed that Slamf9 overexpression led to a substantial increase in M1 macrophage marker expression and a significant decrease in M2 macrophage marker expression (Fig. 9C-D). These findings indicate that Slamf9 can counteract the effect of DSCM@EVs on M1 macrophage reprogramming.

Subsequently, we investigated whether Slamf9 regulation of M1 macrophage reprogramming influences NSCs differentiation. Co-culturing M1 macrophages overexpressing or lacking Slamf9 with DSCM@EVs confirmed the impact through functional validation in the NSCs culture medium. Results revealed that Slamf9 overexpression inhibited NSCs proliferation and migration while promoting differentiation into astrocytes, and inhibiting neuronal axon formation (Fig. 9E-J). Additionally, knocking down Slamf9 in M1 macrophages was validated, and the lower efficiency sh-Slamf9#1 (sh-Slamf9) was chosen for verification (Figure S7A). Experimental outcomes showed that Slamf9 knockdown promoted M1 macrophage reprogramming and NSCs differentiation (Figure S7B-I).

In conclusion, DSCM@EVs inhibit Slamf9 expression in M1 macrophages, promoting M2 reprogramming and accelerating NSCs differentiation.

Discussion

This study reveals the significant potential of DSCM hydrogel functionalized with DSCM@EVs in the treatment of SCI. Specifically, DSCM@EVs can promote the reprogramming of macrophages (primarily M1 type)

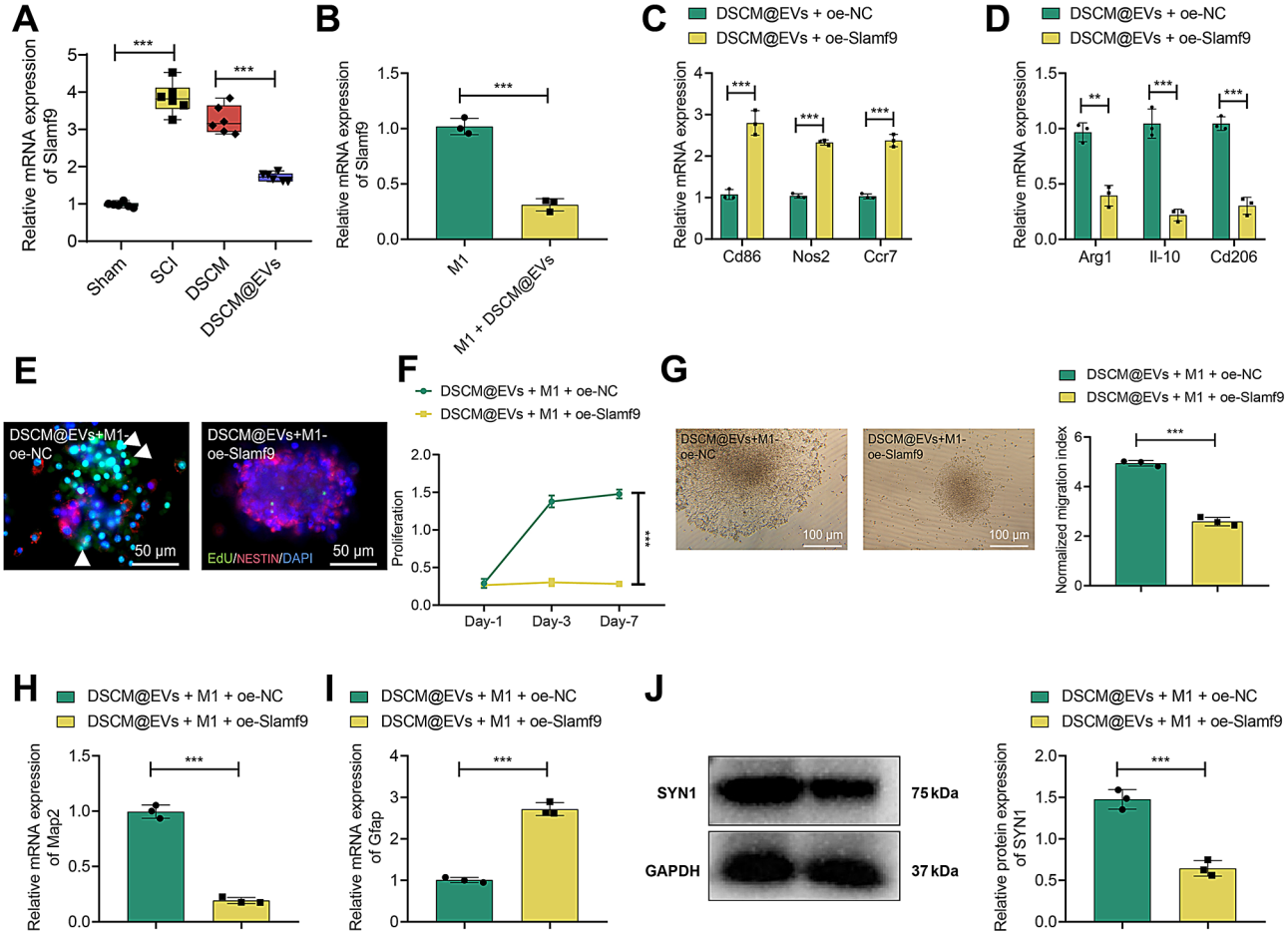

Fig. 9 DSCM@EVs Mediate Slamf9 Regulation of M1 Macrophage Reprogramming Affecting NSC Differentiation. Note: (**A**) Gene expression levels of Slamf9 in spinal cord tissues of mice in each group were examined by RT-qPCR, with 6 mice per group; (**B**) Slamf9 gene expression levels in M1 macrophages from each group were detected by RT-qPCR; (**C**-**D**) Following co-incubation of DSCM@EVs with M1 macrophages overexpressing or not overexpressing Slamf9, gene expression levels of M1 macrophage markers Nos2, Ccr7, and Cd86, as well as M2 macrophage markers Arg1, Cd206, and Il-10, were assessed by RT-qPCR; (**E**) M1 macrophages co-incubated or not with DSCM@EVs were used for CM collection for NSC incubation (White arrows), EdU staining was performed to evaluate NSC proliferation, with DAPI staining of nuclei in blue, NESTIN staining of NSCs in red, and EdU staining of proliferating NSCs in green, scale bar = 50 μm; (**F**) NSC proliferation in each group was measured using CCK-8 assay; (**G**) Migration of NSCs in each group was assessed, with red dashed lines as reference, scale bar = 100 μm; (**H**-**I**) Gene expression levels of neuronal and astroglial cell markers in NSCs from each group were determined by RT-qPCR; (**J**) SYN1 protein expression levels, a marker of neuronal axons, in NSCs from each group were evaluated by Western blot. * denotes comparison between two groups, $P < 0.05$, and cell experiments were repeated at least three times

towards the M2 phenotype by downregulating Slamf9 expression, thereby improving the inflammatory environment in the SCI region. This alteration facilitates the proliferation, migration, differentiation, and axonal growth of NSCs, ultimately aiming to alleviate the progression of SCI.

SCI has been a focal point in the medical field, given its direct impact on patients' quality of life and survival rates [53]. Traditional therapeutic approaches, such as medication and surgery, often only provide symptom relief rather than addressing the root cause [54]. With the rapid advancement of bioengineering and cell therapies, researchers have begun exploring the use of stem cells and biomaterials to enhance the regeneration and repair of neural tissues [55, 56]. However, these methods are frequently impeded by issues like biocompatibility and stem cell safety [57]. In contrast to existing studies, we are introducing DSCM@EVs composite material as a novel therapeutic strategy for the first time here.

Macrophages play pivotal biological roles in SCI and other inflammatory diseases [58]. Particularly, M1 and M2 macrophages exhibit distinct functions in inflammatory responses and tissue repair [59]. Most current research focuses on inhibiting M1 macrophage activity or enhancing M2 function [60]. However, these studies often lack precise regulatory mechanisms [61, 62]. In contrast, our study identifies that precise promotion of macrophage transition from M1 to M2 can be achieved by downregulating Slamf9.

In the process of neural repair, DSCM and EVs play crucial roles [13, 63]. DSCM is commonly used as an extracellular matrix to promote cell adhesion and proliferation, while EVs are considered effective carriers of signaling molecules [64, 65]. However, the effectiveness of using these methods alone is limited [66]. In this study, we combine DSCM with EVs to form the DSCM@EVs composite material. This design not only enhances the biocompatibility of the material but also boosts its effectiveness in promoting neural repair.

SCI is a common disease of the central nervous system with high disability rates, leading to loss of motor and sensory functions. Current treatment options for SCI are limited, making it crucial to explore innovative methods to enhance the recovery of SCI patients [67]. Previous studies have shown that decellularized spinal cord matrix (DSCM), derived from spinal cord tissue and retaining natural biological structure and bioactive molecules after decellularization, possesses the potential to induce nerve regeneration and repair. DSCM can serve as an injectable hydrogel to support the proliferation and differentiation of NSCs, promoting axonal regeneration and neuronal connectivity [13]. MSC-derived EVs, a type of cellular EVs, are widely used in regenerative medicine to modulate intercellular communication and signaling by carrying bioactive molecules. These EVs improve central nervous system functions, such as neurogenesis and angiogenesis, to enhance the repair of spinal cord injuries. Additionally, they have the ability to regulate immune cell activity, holding significant potential as a cell-free therapy for SCI repair and regeneration, garnering significant attention in recent years [67, 68]. The combination of EVs and hydrogels presents great potential in SCI treatment. This integrated hydrogel, when combined with DSCM@EVs, can provide the bioactive molecules necessary to support nerve repair and regeneration, creating a favorable microenvironment within damaged neural tissues. Compared to EVs used in conjunction with hydrogels, the release rate and bioactivity of EVs in this combination are easier to control, thereby enhancing treatment controllability and effectiveness. These innovative approaches not only improve therapeutic outcomes but also offer better rehabilitation opportunities for SCI patients. Therefore, further research and clinical application of these novel methods are highly important and hold promise for bringing breakthroughs and advancements in SCI treatment.

Compared to previous research, this study presents multiple innovations. First, we successfully combined DSCM with EVs to create a novel composite material, introducing a breakthrough with promising potential for SCI treatment. Additionally, we uncovered a new molecular mechanism in which DSCM@EVs modulate Slamf9 expression in M1 macrophages, promoting their reprogramming to M2 macrophages. This reprogramming reduces the inflammatory environment in the SCI region, fostering NSCs' proliferation, migration, differentiation, and axon growth, which collectively aid in alleviating SCI progression. This mechanism holds significance not only for SCI treatment but also for other inflammatory diseases.

However, some limitations and challenges remain in this study. Firstly, all experimental results were obtained from mouse models, and further validation is required to determine their applicability in humans. Moreover, this study focuses primarily on short-term therapeutic effects; long-term outcomes and potential side effects remain unclear. While we identified Slamf9's role in macrophage polarization, additional research is needed to investigate other molecules and pathways potentially involved in this process. Additionally, the variability in the bioactivity of MSC-derived EVs, influenced by differing cellular states and conditions, warrants further exploration. Factors like the MSC's differentiation status and environmental influences (e.g., hypoxia or inflammation) could impact EV composition, and isolation techniques may affect purity and bioactivity [69].

Given the promising clinical potential of DSCM@EVs, future research will emphasize verifying this composite material's biocompatibility and stability across various cell types, as cell compatibility is crucial for safe in vivo applications. A highly biocompatible material, such as decellularized bovine meninges-derived hydrogel (MeninGEL), which supports mesenchymal stem cell differentiation into neural lineages at physiological temperatures, demonstrates the value of this focus [70]. Our future studies will also continue investigating Slamf9 and other potential molecular targets in depth, aiming to optimize therapeutic strategies and advance them toward clinical application.

This study may also provide insights into treatments for other neurological diseases, such as brain injuries and multiple sclerosis. Specifically, the strategy of macrophage reprogramming represents a novel therapeutic approach, expanding this research's scope and providing interdisciplinary insights.

In conclusion, this study offers a novel perspective for SCI treatment and broadens macrophage reprogramming's application in various inflammatory diseases (Fig. 10). We believe that utilizing DSCM@EVs and targeting Slamf9 for macrophage reprogramming holds significant promise as a therapeutic strategy for SCI and related conditions.

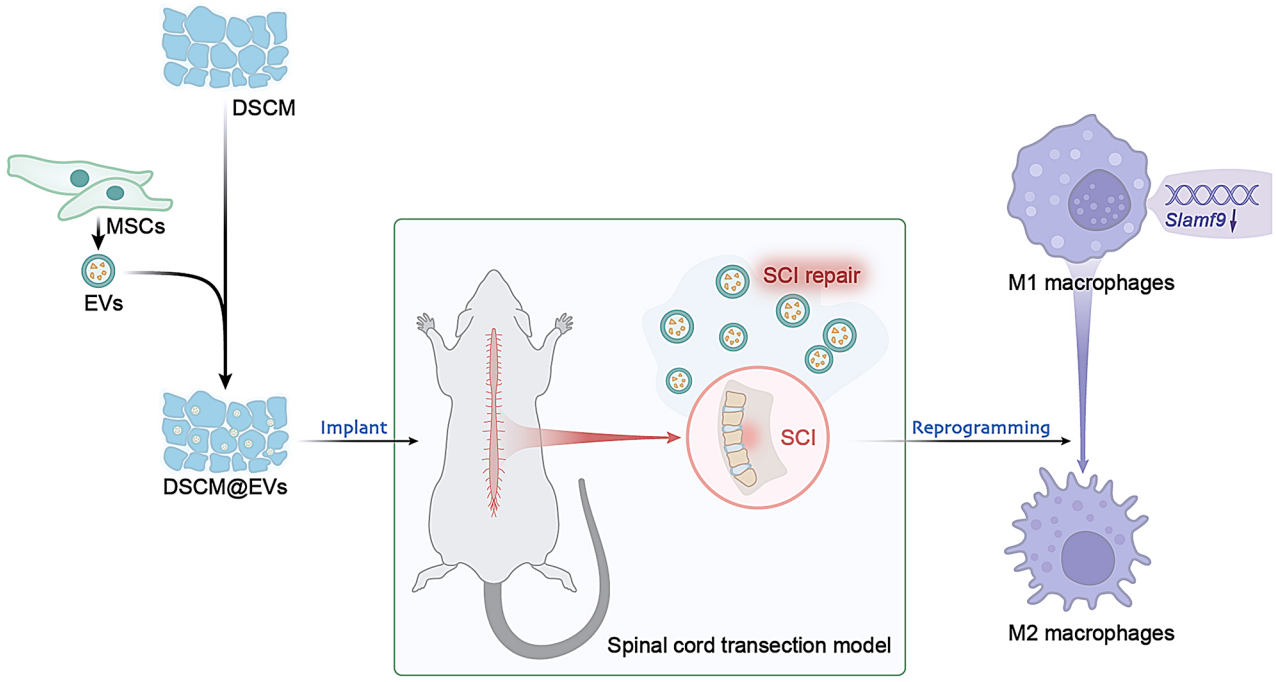

Fig. 10 Schematic Representation of the Mechanism by Which Acellular Matrix Hydrogel Functionalized with EVs Regulates Slamf9 Expression to Modulate M1 Macrophage Reprogramming, Influencing Neural Stem Cell Differentiation in SCI

Supplementary Information

The online version contains supplementary material available at https://doi.org/10.1186/s12951-025-03152-0.

Supplementary Material 1: Figure S1 Characterization of EVs and DSCM Derived from Mouse Spinal Cord MSCs.Note: (A) Flow cytometry to detect the expression of MSC markers; (B) Alizarin Red, Oil Red O, and Alcian Blue staining to assess the osteogenic, adipogenic, and chondrogenic differentiation abilities of MSCs, scale bar = 50 μm; (C) TEM observation of EVs morphology, scale bar = 100 nm; (D) NTA analysis of EVs size; (E) Western blot to examine the expression of EVs markers; (F) H&E staining to evaluate the nuclear signal in NSCM and DSCM, Scale bars = 25 μm; (G) Quantification of DNA content in NSCM and DSCM; (H) Quantification of collagen and GAG content in DNM and DSCM groups; (I) Western blot of collagen and other related ECM protein components. (J) SEM observation of DSCM morphology, scale bars = 5 μm; (K) Calculation of DSCM porosity and nanofiber diameter based on (J); (L) Mechanical properties of gelled DSCM, including gelation time and storage modulus. * indicates a significant difference the between two groups, $P < 0.05$, experiments were performed at least three times.

Supplementary Material 2: Figure S2 Batch Correction of Merged Datasets GSE5296 and GSE47681. Note: (A) PCA analysis of the merged datasets GSE5296 and GSE47681 from the GEO database without batch correction; (B) PCA analysis of the merged datasets GSE5296 and GSE47681 from the GEO database after batch correction.

Supplementary Material 3: Figure S3 The Impact of DSCM@EVs on the Viability of NSCs and M1 Macrophages. Note: (A) Morphological observation of NSCs under a light microscope, scale bar = 50 μm; (B) Immunofluorescence co-staining for the purity evaluation of NSCs, scale bar = 25 μm; (C) Positive rates of SOX2 and NESTIN in Figure B; (D) Detection of NSC viability through live/dead cell staining, scale bar = 25 μm; (E) NSC viability percentage in Figure D; (F) Ratio of live to dead NSCs in Figure D. Cell experiments were repeated at least three times.

Supplementary Material 4: Figure S4 Effects of Different Macrophages on NSC Differentiation. Note: NSCs were incubated with CM from different types of macrophages. (A) Cell Counting Kit-8 (CCK-8) was used to assess the proliferation of NSCs in each group; (B) Migration assay was conducted to evaluate the migration of NSCs in each group, scale bar = 100 μm; (C-D) RT-qPCR was performed to measure the gene expression levels of neural and glial cell markers in NSCs from each group; (E) Western blot analysis was carried out to examine the protein expression levels of neuronal axonal markers in NSCs from each group. * indicates comparison between two groups, $P < 0.05$, ** $P < 0.01$, and cell experiments were repeated at least three times.

Supplementary Material 5: Figure S5 Analysis of Differentially Expressed Genes in RNA-seq. Note: (A) Bar chart of RNA-seq sample data before standardization; (B) Bar chart of RNA-seq sample data after standardization; (C) Heat map showing the expression of 120 differentially expressed genes in RNA-seq data; (D) In the RNA-seq data, 120 differentially expressed genes are represented with black indicating non-differentially expressed genes, red indicating upregulated genes, and green indicating downregulated genes. Each group consists of 3 sample instances.

Supplementary Material 6: Figure S6 Enrichment Analysis of Differentially Expressed Genes in RNA-seq. Note: (A) Bubble chart displaying GO enrichment of 3178 differentially expressed genes; (B) Circular plot illustrating KEGG enrichment of 3178 differentially expressed genes; (C) GSEA enrichment plot of 3178 differentially expressed genes.

Supplementary Material 7: Figure S7 Slamf9 Regulates the Reprogramming of M1 Macrophages and Its Impact on NSC Differentiation. Note: (A) Efficiency of Slamf9 knockdown detected by RT-qPCR; (B-C) Gene expression levels of M1 macrophage markers Nos2, Ccr7, and Cd86, as well as M2 macrophage markers Arg1, Cd206, and Il-10, detected by RT-qPCR in the respective groups; (D) Proliferation of NSCs in each group assessed by EdU staining, with blue indicating DAPI-stained nuclei, red representing NESTIN-stained NSCs, and green showing EdU-labeled proliferating NSCs, scale bar = 50 μm; (E) Proliferation of NSCs in each group determined by CCK-8 assay; (F) Migration of NSCs in each group, scale bar = 100 μm; (G-H) Gene expression levels of neuronal and astrocytic markers in NSCs detected by RT-qPCR in the respective groups; (I) Protein expression levels of neuronal axon marker SYN1 in NSCs from each group assessed by Western blot. * indicates statistical significance between the two groups, with

$P < 0.05$, and cell experiments were repeated at least three times.

Supplementary Material 8

Acknowledgements
None.

Author contributions
Ming Deng and Ping Xie: Conceptualized and designed the study, performed data analysis, and wrote the manuscript.Hongyang Xue and Qing Chen: Conducted experiments, including the isolation of extracellular vesicles and preparation of DSCM hydrogels, and contributed to manuscript drafting. Yan Zhou and Jianghua Ming: Performed in vivo and in vitro experiments, including mouse SCI modeling and macrophage reprogramming assays, and contributed to data collection.Yonggang Ma and Junqi Liu: Performed bioinformatics analyses, including RNA-seq data processing and identification of key regulatory genes, and contributed to data interpretation.Hui Huang: Supervised the overall study, provided critical feedback on the manuscript, and served as the corresponding author.All authors: Reviewed and approved the final version of the manuscript.

Funding
This study was supported by Natural Science Foundation of Hubei Province (No. 2019CFB457), Innovative Seed Funds of Medical College of Wuhan University (No. TFZZ2018027), and Wuhan Medical Research Project (Youth Project) (No. WZ19Q02).

Data availability
No datasets were generated or analysed during the current study.

Declarations

Ethical approval
All animal experiments were approved by the Animal Ethics Committee. The study does not involve any clinical ethics considerations.

Competing interests
The authors declare no competing interests.

Received: 30 July 2024 / Accepted: 22 January 2025
Published online: 25 February 2025

References

1. Panicker JN. Neurogenic bladder: epidemiology, diagnosis, and management. Semin Neurol. 2020;40(5):569–79. https://doi.org/10.1055/s-0040-1713876.
2. She Y, Zhao X, Wu P et al. COL8A1 predicts the clinical prognosis of gastric Cancer and is related to epithelial-mesenchymal transition. Biomed Res Int. 2022;2022:7567447. Published 2022 Jun 21. https://doi.org/10.1155/2022/7567447
3. Sidwell RA. Intraoperative Teaching and evaluation in general surgery. Surg Clin North Am. 2021;101(4):587–95. https://doi.org/10.1016/j.suc.2021.05.006.
4. Xiao X, Li W, Xu Z, et al. Extracellular vesicles from human umbilical cord mesenchymal stem cells reduce lipopolysaccharide-induced spinal cord injury neuronal apoptosis by mediating miR-29b-3p/PTEN. Connect Tissue Res. 2022;63(6):634–49. https://doi.org/10.1080/03008207.2022.2060826.
5. Ghane N, Beigi MH, Labbaf S, Nasr-Esfahani MH, Kiani A. Design of hydrogel-based scaffolds for the treatment of spinal cord injuries. J Mater Chem B. 2020;8(47):10712–38. https://doi.org/10.1039/d0tb01842b.
6. Gao L, Peng Y, Xu W, et al. Progress in Stem Cell Therapy for spinal cord Injury. Stem Cells Int. 2020. https://doi.org/10.1155/2020/2853650. 2020:2853650. Published 2020 Nov 5.
7. Rhode SC, Beier JP, Ruhl T. Adipose tissue stem cells in peripheral nerve regeneration-In vitro and in vivo. J Neurosci Res. 2021;99(2):545–60. https://doi.org/10.1002/jnr.24738.
8. Ulldemolins A, Jurado A, Herranz-Diez C, et al. Lung extracellular matrix hydrogels-derived vesicles contribute to epithelial lung repair. Polym (Basel). 2022;14(22):4907. https://doi.org/10.3390/polym14224907. Published 2022 Nov 14.
9. Liu S, Wu X, Chandra S, et al. Extracellular vesicles: emerging tools as therapeutic agent carriers. Acta Pharm Sin B. 2022;12(10):3822–42. https://doi.org/10.1016/j.apsb.2022.05.002.
10. Wang R, Wang X, Zhang Y, et al. Emerging prospects of extracellular vesicles for brain disease theranostics. J Control Release. 2022;341:844–68. https://doi.org/10.1016/j.jconrel.2021.12.024.
11. Jiang W, Xu Y, Chen JC, et al. Role of extracellular vesicles in nonalcoholic fatty liver disease. Front Endocrinol (Lausanne). 2023;14:1196831. https://doi.org/10.3389/fendo.2023.1196831. Published 2023 Jul 18.
12. He J, Liu J, Huang Y, Lan Z, Tang X, Hu Z. Mesenchymal stem cells-derived therapies for subarachnoid hemorrhage in preclinical rodent models: a meta-analysis. Stem Cell Res Ther. 2022;13(1):42. https://doi.org/10.1186/s13287-022-02725-2. Published 2022 Jan 29.
13. Xu Y, Zhou J, Liu C, et al. Understanding the role of tissue-specific decellularized spinal cord matrix hydrogel for neural stem/progenitor cell microenvironment reconstruction and spinal cord injury. Biomaterials. 2021;268:120596. https://doi.org/10.1016/j.biomaterials.2020.120596.
14. Xie Z, Shen Z, Zhan P, et al., et al. Functional Dental Pulp Regeneration: Basic Research and clinical translation. Int J Mol Sci. 2021;22(16):8991. https://doi.org/10.3390/ijms22168991. Published 2021 Aug 20.
15. Yin B, Ni J, Witherel CE, et al. Harnessing tissue-derived Extracellular vesicles for Osteoarthritis Theranostics. Theranostics. 2022;12(1):207–31. https://doi.org/10.7150/thno.62708. Published 2022 Jan 1.
16. Chen Z, Hu Z, Sui Q, et al. LncRNA FAM83A-AS1 facilitates tumor proliferation and the migration via the HIF-1α/ glycolysis axis in lung adenocarcinoma. Int J Biol Sci. 2022;18(2):522–35. https://doi.org/10.7150/ijbs.67556. Published 2022 Jan 1.
17. Wan J, Liu B. Construction of lncRNA-related ceRNA regulatory network in diabetic subdermal endothelial cells. Bioengineered. 2021;12(1):2592–602. https://doi.org/10.1080/21655979.2021.1936892.
18. Zhao Y, Wang L, Wu Y, Lu Z, Zhang S. Genome-wide study of key genes and scoring system as potential noninvasive biomarkers for detection of suicide behavior in major depression disorder. Bioengineered. 2020;11(1):1189–96. https://doi.org/10.1080/21655979.2020.1831349.
19. Li T, Wang W, Gan W, et al. Comprehensive bioinformatics analysis identifies LAPTM5 as a potential blood biomarker for hypertensive patients with left ventricular hypertrophy. Aging. 2022;14(3):1508–28. https://doi.org/10.18632/aging.203894.
20. Butler A, Hoffman P, Smibert P, Papalexi E, Satija R. Integrating single-cell transcriptomic data across different conditions, technologies, and species. Nat Biotechnol. 2018;36(5):411–20. https://doi.org/10.1038/nbt.4096.
21. Mistry P, Nakabo S, O'Neil L, et al. Transcriptomic, epigenetic, and functional analyses implicate neutrophil diversity in the pathogenesis of systemic lupus erythematosus. Proc Natl Acad Sci U S A. 2019;116(50):25222–8. https://doi.org/10.1073/pnas.1908576116.
22. Yu G, Wang LG, Han Y, He QY. clusterProfiler: an R package for comparing biological themes among gene clusters. OMICS. 2012;16(5):284–7. https://doi.org/10.1089/omi.2011.0118.
23. Wen F, Lu X, Huang W, et al. Characteristics of immunophenotypes and immunological in tumor microenvironment and analysis of immune implication of CXCR4 in gastric cancer. Sci Rep. 2022;12(1):5720. https://doi.org/10.1038/s41598-022-08622-1. Published 2022 Apr 6.
24. Jin J, Ou Q, Wang Z et al. BMSC-derived extracellular vesicles intervened the pathogenic changes of scleroderma in mice through miRNAs. Stem Cell Res Ther. 2021;12(1):327. Published 2021 Jun 5. https://doi.org/10.1186/s13287-021-02400-y
25. Yan W, Wu X, Zhou W, et al. Cancer-cell-secreted exosomal miR-105 promotes tumour growth through the MYC-dependent metabolic reprogramming of stromal cells. Nat Cell Biol. 2018;20(5):597–609. https://doi.org/10.1038/s41556-018-0083-6.
26. Jiang Y, Wang R, Wang C, et al. Brain microenvironment responsive and pro-angiogenic extracellular vesicle-hydrogel for promoting Neurobehavioral Recovery in type 2 Diabetic mice after stroke. Adv Healthc Mater. 2022;11(22):e2201150. https://doi.org/10.1002/adhm.202201150.
27. Strader MK, Katz BM, Stanton CM. Student recruitment: a report of significant gains through systematic construction of a persuasive communication. J Prof Nurs. 1987;3(6):354–61. https://doi.org/10.1016/s8755-7223(87)80124-2.
28. Yang Y, Fan Y, Zhang H, et al. Small molecules combined with collagen hydrogel direct neurogenesis and migration of neural stem cells after spinal cord

injury. Biomaterials. 2021;269:120479. https://doi.org/10.1016/j.biomaterials.2020.120479.
29. Cho DI, Kim MR, Jeong HY, et al. Mesenchymal stem cells reciprocally regulate the M1/M2 balance in mouse bone marrow-derived macrophages. Exp Mol Med. 2014;46(1):e70. https://doi.org/10.1038/emm.2013.135. Published 2014 Jan 10.
30. Zhang K, Zheng J, Bian G, et al. Polarized macrophages have distinct roles in the differentiation and Migration of embryonic spinal-cord-derived neural stem cells after grafting to Injured sites of spinal cord. Mol Ther. 2015;23(6):1077–91. https://doi.org/10.1038/mt.2015.46.
31. Xiao X, Lu Z, Lin V, et al. MicroRNA Mir-24-3p reduces apoptosis and regulates Keap1-Nrf2 pathway in mouse cardiomyocytes responding to Ischemia/Reperfusion Injury. Oxid Med Cell Longev. 2018;2018:7042105. https://doi.org/10.1155/2018/7042105. Published 2018 Dec 2.
32. Li H, Wang X, Wen C, et al. Long noncoding RNA NORAD, a novel competing endogenous RNA, enhances the hypoxia-induced epithelial-mesenchymal transition to promote metastasis in pancreatic cancer. Mol Cancer. 2017;16(1):169. https://doi.org/10.1186/s12943-017-0738-0. Published 2017 Nov 9.
33. Zhang Z, Yin J, Lu C, Wei Y, Zeng A, You Y. Exosomal transfer of long non-coding RNA SBF2-AS1 enhances chemoresistance to temozolomide in glioblastoma. J Exp Clin Cancer Res. 2019;38(1):166. https://doi.org/10.1186/s13046-019-1139-6. Published 2019 Apr 16.
34. Fan L, Liu C, Chen X, et al. Directing Induced pluripotent stem cell derived neural stem cell fate with a three-Dimensional Biomimetic Hydrogel for spinal cord Injury Repair. ACS Appl Mater Interfaces. 2018;10(21):17742–55. https://doi.org/10.1021/acsami.8b05293.
35. Luo F, Wang J, Zhang Z, et al. Inhibition of CSPG receptor PTPσ promotes migration of newly born neuroblasts, axonal sprouting, and recovery from stroke. Cell Rep. 2022;40(4):111137. https://doi.org/10.1016/j.celrep.2022.111137.
36. Cheriyan T, Ryan DJ, Weinreb JH, et al. Spinal cord injury models: a review. Spinal Cord. 2014;52(8):588–95. https://doi.org/10.1038/sc.2014.91.
37. Irrera N, Arcoraci V, Mannino F et al. Activation of A2A Receptor by PDRN Reduces Neuronal Damage and Stimulates WNT/β-CATENIN Driven Neurogenesis in Spinal Cord Injury [published correction appears in Front Pharmacol. 2022;13:1073726. doi: 10.3389/fphar.2022.1073726]. Front Pharmacol. 2018;9:506. Published 2018 May 29. https://doi.org/10.3389/fphar.2018.00506
38. Noristani HN, Gerber YN, Sabourin JC, et al. RNA-Seq Analysis of Microglia Reveals Time-Dependent Activation of Specific Genetic Programs following spinal cord Injury. Front Mol Neurosci. 2017;10:90. https://doi.org/10.3389/fnmol.2017.00090. Published 2017 Apr 3.
39. Li J, Liu C, Chen Y, et al. Tumor characterization in breast Cancer identifies Immune-relevant Gene signatures Associated with Prognosis. Front Genet. 2019;10:1119. https://doi.org/10.3389/fgene.2019.01119. Published 2019 Nov 12.
40. Garikipati VNS, Verma SK, Cheng Z et al. Circular RNA CircFndc3b modulates cardiac repair after myocardial infarction via FUS/VEGF-A axis [published correction appears in Nat Commun. 2020;11(1):2234. doi: 10.1038/s41467-020-15382-x]. Nat Commun. 2019;10(1):4317. Published 2019 Sep 20. https://doi.org/10.1038/s41467-019-11777-7
41. Ayuk SM, Abrahamse H, Houreld NN. The role of photobiomodulation on gene expression of cell adhesion molecules in diabetic wounded fibroblasts in vitro. J Photochem Photobiol B. 2016;161:368–74. https://doi.org/10.1016/j.jphotobiol.2016.05.027.
42. Wu Q, Yi X. Down-regulation of long noncoding RNA MALAT1 protects hippocampal neurons against excessive autophagy and apoptosis via the PI3K/Akt Signaling Pathway in rats with Epilepsy. J Mol Neurosci. 2018;65(2):234–45. https://doi.org/10.1007/s12031-018-1093-3.
43. Ma S, Mangala LS, Hu W, et al. CD63-mediated cloaking of VEGF in small extracellular vesicles contributes to anti-VEGF therapy resistance. Cell Rep. 2021;36(7):109549. https://doi.org/10.1016/j.celrep.2021.109549.
44. Thuret S, Moon LD, Gage FH. Therapeutic interventions after spinal cord injury [published correction appears in nat Rev Neurosci. 2006;7(11):902]. Nat Rev Neurosci. 2006;7(8):628–43. https://doi.org/10.1038/nrn1955.
45. Dutta D, Khan N, Wu J, Jay SM. Extracellular vesicles as an emerging Frontier in spinal cord Injury Pathobiology and Therapy. Trends Neurosci. 2021;44(6):492–506. https://doi.org/10.1016/j.tins.2021.01.003.
46. Park J, Zhang Y, Saito E, et al. Intravascular innate immune cells reprogrammed via intravenous nanoparticles to promote functional recovery after spinal cord injury. Proc Natl Acad Sci U S A. 2019;116(30):14947–54. https://doi.org/10.1073/pnas.1820276116.
47. Kroner A, Greenhalgh AD, Zarruk JG, Passos Dos Santos R, Gaestel M, David S. TNF and increased intracellular iron alter macrophage polarization to a detrimental M1 phenotype in the injured spinal cord. Neuron. 2014;83(5):1098–116. https://doi.org/10.1016/j.neuron.2014.07.027.
48. Orecchioni M, Ghosheh Y, Pramod AB, Ley K. Macrophage Polarization: Different Gene Signatures in M1(LPS+) vs. Classically and M2(LPS-) vs. Alternatively Activated Macrophages [published correction appears in Front Immunol. 2020;11:234. doi: 10.3389/fimmu.2020.00234]. Front Immunol. 2019;10:1084. Published 2019 May 24. https://doi.org/10.3389/fimmu.2019.01084
49. Luo X, Dai M, Wang M, Wang X, Guo W. Functional heterogeneity of wnt-responsive and hedgehog-responsive neural stem cells in the murine adult hippocampus. Dev Cell. 2023;58(22):2545–e25626. https://doi.org/10.1016/j.devcel.2023.07.021.
50. Perlini LE, Botti F, Fornasiero EF, et al. Effects of phosphorylation and neuronal activity on the control of synapse formation by synapsin I. J Cell Sci. 2011;124(Pt 21):3643–53. https://doi.org/10.1242/jcs.086223.
51. Murphy MK, Moon JT, Skolaris AT, Mikulin JA, Wilson TJ. Evidence for the loss and recovery of SLAMF9 during human evolution: implications on Dollo's law. Immunogenetics. 2021;73(3):243–51. https://doi.org/10.1007/s00251-021-01208-7.
52. Sever L, Radomir L, Stirm K et al. SLAMF9 regulates pDC homeostasis and function in health and disease [published correction appears in Proc Natl Acad Sci U S A. 2019;116(39):19760. doi: 10.1073/pnas.1914890116]. Proc Natl Acad Sci U S A. 2019;116(33):16489–16496. https://doi.org/10.1073/pnas.1900079116
53. Cramer MN, Gagnon D, Laitano O, Crandall CG. Human temperature regulation under heat stress in health, disease, and injury. Physiol Rev. 2022;102(4):1907–89. https://doi.org/10.1152/physrev.00047.2021.
54. Li C, Sun T, Jiang C. Recent advances in nanomedicines for the treatment of ischemic stroke. Acta Pharm Sin B. 2021;11(7):1767–88. https://doi.org/10.1016/j.apsb.2020.11.019.
55. Klionsky DJ, Abdel-Aziz AK, Abdelfatah S et al. Guidelines for the use and interpretation of assays for monitoring autophagy (4th edition)[1]. Autophagy. 2021;17(1):1-382. https://doi.org/10.1080/15548627.2020.1797280
56. Pušić T, Šaravanja B, Malarić K. Electromagnetic Shielding properties of Knitted Fabric made from Polyamide threads coated with Silver. Mater (Basel). 2021;14(5):1281. https://doi.org/10.3390/ma14051281. Published 2021 Mar 8.
57. Onwuka E, King N, Heuer E, Breuer C. The heart and great vessels. Cold Spring Harb Perspect Med. 2018;8(3):a031922. https://doi.org/10.1101/cshperspect.a031922. Published 2018 Mar 1.
58. Henein MY, Vancheri S, Longo G, Vancheri F. The role of inflammation in Cardiovascular Disease. Int J Mol Sci. 2022;23(21):12906. https://doi.org/10.3390/ijms232112906. Published 2022 Oct 26.
59. Fernandes TL, Gomoll AH, Lattermann C, Hernandez AJ, Bueno DF, Amano MT. Macrophage: a potential target on cartilage regeneration. Front Immunol. 2020;11:111. https://doi.org/10.3389/fimmu.2020.00111. Published 2020 Feb 11.
60. Yamagishi A, Nakajima H, Kokubo Y, Yamamoto Y, Matsumine A. Polarization of infiltrating macrophages in the outer annulus fibrosus layer associated with the process of intervertebral disc degeneration and neural ingrowth in the human cervical spine. Spine J. 2022;22(5):877–86. https://doi.org/10.1016/j.spinee.2021.12.005.
61. Moraitis AM, Seven M, Walker RK. Physical activity in Young Adult Cancer survivors: a scoping review. Oncol Nurs Forum. 2021;48(2):184–94. https://doi.org/10.1188/21.ONF.184-194.
62. Pezzanite LM, Chow L, Griffenhagen GM, et al. Distinct differences in immunological properties of equine orthobiologics revealed by functional and transcriptomic analysis using an activated macrophage readout system. Front Vet Sci. 2023;10:1109473. https://doi.org/10.3389/fvets.2023.1109473. Published 2023 Feb 16.
63. Flagiello D, Erto A, Lancia A, Di Natale F. Dataset of wet desulphurization scrubbing in a column packed with mellapak 250.X. Data Brief. 2020;33:106383. https://doi.org/10.1016/j.dib.2020.106383. Published 2020 Oct 8.
64. Pérez-Castrillo S, González-Fernández ML, López-González ME, Villar-Suárez V. Effect of ascorbic and chondrogenic derived decellularized extracellular matrix from mesenchymal stem cells on their proliferation, viability and differentiation. Ann Anat. 2018;220:60–9. https://doi.org/10.1016/j.aanat.2018.07.006.
65. Adeleke AA, Ikubanni PP, Orhadahwe TA, et al. Sustainability of multifaceted usage of biomass: a review. Heliyon. 2021;7(9):e08025. https://doi.org/10.1016/j.heliyon.2021.e08025. Published 2021 Sep 20.

66. Mursch-Edlmayr AS, Luft N, Podkowinski D, Ring M, Schmetterer L, Bolz M. Differences in Optic nerve Head Blood Flow Regulation in normal tension Glaucoma patients and healthy controls as assessed with laser Speckle Flowgraphy during the Water drinking test. J Glaucoma. 2019;28(7):649–54. https://doi.org/10.1097/IJG.0000000000001258.
67. Wang S, Du C, Li G. Mesenchymal stem cell-derived extracellular vesicles: emerging concepts in the treatment of spinal cord injury. Am J Transl Res. 2023;15(7):4425–38. Published 2023 Jul 15.
68. Afsartala Z, Hadjighassem M, Shirian S, et al. Advances in management of spinal cord Injury using stem cell-derived Extracellular vesicles: a review study. Basic Clin Neurosci. 2023;14(4):443–51. https://doi.org/10.32598/bcn.2022.3430.2.
69. Kim JY, Rhim WK, Yoo YI, et al. Defined MSC exosome with high yield and purity to improve regenerative activity. J Tissue Eng. 2021;12:20417314211008626. https://doi.org/10.1177/20417314211008626. Published 2021 Apr 20.
70. Ozudogru E, Isik M, Eylem CC, Nemutlu E, Arslan YE, Derkus B. Decellularized spinal cord meninges extracellular matrix hydrogel that supports neurogenic differentiation and vascular structure formation. J Tissue Eng Regen Med. 2021;15(11):948–63. https://doi.org/10.1002/term.3240.

Publisher's note